HHS Public Access

Author manuscript

Mol Cell. Author manuscript; available in PMC 2024 August 03.

Published in final edited form as:

Mol Cell. 2023 August 03; 83(15): 2692–2708.e7. doi:10.1016/j.molcel.2023.06.024.

A lncRNA from the *FTO* locus acts as a suppressor of the m^{6}A writer complex and p53 tumor suppression signaling

Jianong Zhang[1,4,#,*], **Jiangbo Wei**[2,3,#], **Rui Sun**[1,#], **Haoyue Sheng**[1], **Kai Yin**[1,5], **Yunqian Pan**[1], **Rafael Jimenez**[6], **Sujun Chen**[7], **Xiao-long Cui**[2,3], **Zhongyu Zou**[2,3], **Zhiying Yue**[8], **Michael J. Emch**[1], **John R. Hawse**[1], **Liguo Wang**[9], **Housheng Hansen He**[7], **Shujie Xia**[4], **Bangmin Han**[4], **Chuan He**[2,3,*], **Haojie Huang**[1,10,*]

[1]Department of Biochemistry and Molecular Biology, Mayo Clinic, 200 First Street SW, Rochester, MN, 55905, USA

[2]Department of Chemistry, Department of Biochemistry and Molecular Biology, and Institute for Biophysical Dynamics, The University of Chicago, 929 East 57th Street, Chicago, IL, 60637, USA

[3]Howard Hughes Medical Institute, The University of Chicago, 929 East 57th Street, Chicago, IL, 60637, USA

[4]Department of Urology, Shanghai General Hospital, Shanghai Jiao Tong University School of Medicine, No. 100 Haining Road, Hongkou District, Shanghai, 200080, China

[5]Department of General Surgery, Affiliated Hospital of Jiangsu University, Zhenjiang, 212002, China

[6]Department of Laboratory Medicine and Pathology, Mayo Clinic College of Medicine and Science, Rochester, MN 55905

[7]Princess Margaret Cancer Centre, University Health Network, Toronto, ON M5G 1L7, Canada

[8]Precision Research Center for Refractory Diseases, Shanghai General Hospital, Shanghai Jiao Tong University School of Medicine, Shanghai, 201620, China.

[9]Department of Computation Biology, Mayo Clinic College of Medicine and Science, Rochester, MN 55905, USA

[10]Lead Contact

Summary

[*]**Correspondence**: huang.haojie@mayo.edu (Haojie Huang), chuanhe@uchicago.edu (Chuan He), hugebox@qq.com (Jianong Zhang).

[#]These authors contributed equally.

Author Contributions

H.H. and C.H. conceived the study. J.Z., J.W., R.S., Y.P., Z.Y., M.J.E., J.R.H., S.X., B.H. generated reagents and conducted experiment design and execution, data collection and data analysis. J. W., S.C., H.S., X.C, Z.Z., L.W., H.H.H. performed bioinformatics analysis. R.J. acquired patient samples. H.H., C.H., J.W., J.Z. wrote the manuscript.

Declaration of Interests

The other authors declare no competing interests.

N^6-methyladenosine (m^6A) of mRNAs modulated by the METTL3-METTL14-WTAP-RBM15 methyltransferase complex and m^6A demethylases such as FTO plays important roles in regulating mRNA stability, splicing and translation. Here we demonstrated that *FTO-IT1* lncRNA was upregulated and positively correlated with poor survival of patients with wild-type p53-expressing prostate cancer (PCa). m^6A RIP-seq analysis revealed that *FTO-IT1* knockout increased mRNA m^6A methylation of a subset of p53 transcriptional target genes (e.g. *FAS*, *TP53INP1* and *SESN2*) and induced PCa cell cycle arrest and apoptosis. We further showed that *FTO-IT1* directly binds RBM15 and inhibits RBM15 binding, m^6A methylation and stability of p53 target mRNAs. Therapeutic depletion of *FTO-IT1* restored mRNA m^6A level and expression of p53 target genes and inhibited PCa growth in mice. Our study identifies *FTO-IT1* lncRNA as a *bona fide* suppressor of the m^6A methyltransferase complex and p53 tumor suppression signaling and nominates *FTO-IT1* as a potential therapeutic target of cancer.

eTOC Blurb

Zhang et al. identified *FTO-IT1*, a lncRNA upregulated in antiandrogen- and chemotherapy-resistant prostate cancer as a *bona fide* inhibitor of the m^6A METTL3-METTL14-WTAP-RBM15 'writer' complex that directly interacts with RBM15, inhibits p53 target gene expression and thereby represents a key driver of prostate cancer progression and a viable therapeutic target.

Graphical Abstract

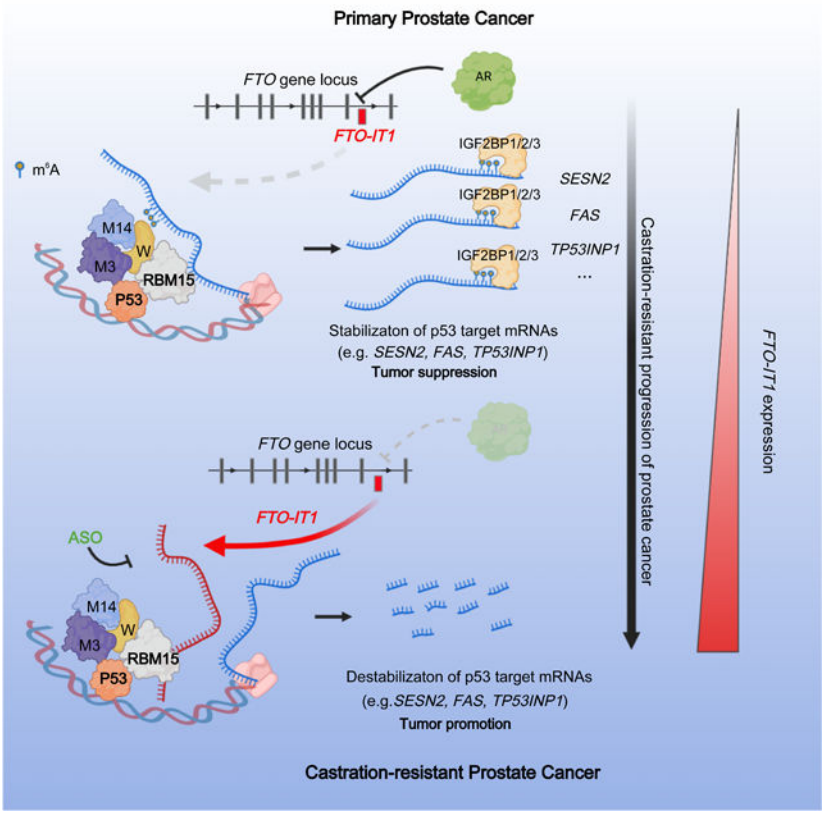

Keywords

FTO-IT1; N^6-methyladenosine; m^6A; p53; RBM15; METTL3; METTL14; lncRNA; prostate cancer

Introduction

N^6-methyladenosine (m^6A) is the most prevalent posttranscriptional modification of RNAs in vertebrate cells Shi et al. [1,2]. This modification is catalyzed by a 'writer' complex comprised primarily of METTL3, METTL14, WTAP and RBM15, in which METTL3 is the methyltransferase (MTase) responsible for casting m^6A, whereas RBM15 and its paralogue RBM15B enable to couple a large number of mRNAs to the 'writer' complex for methylation [3–5]. While RNA m^6A modification is reversible and can be demethylated by demethylases FTO and AlkB homolog 5 (ALKBH5) [6–9], it remains largely unexplored as to how the potent activity of the MTase 'writer' complex itself is regulated, especially by noncoding RNAs (ncRNAs).

The *FTO* gene locus has been identified as an important genomic/epigenomic hub of many biological functions related to cancer and obesity [10–12]. FTO has been linked to cancer and obesity as an RNA m^6A demethylase and a cellular sensor of amino acids and activator of the mammalian target of rapamycin complex 1 (mTORC1) [7,13]. Consistent with the reports that genomic variants such as single nucleotide polymorphisms (SNPs) in introns 1 and 2 of *FTO* gene are strongly associated with the risk of obesity in humans [12,14–16], a few active enhancers have been identified within the SNP regions and linked to the transactivation of obesity-promoting genes [11].

P53 is one of the most important tumor suppressors that safeguards genomic integrity and suppresses oncogenesis. P53 exerts tumor suppressor functions by primarily acting as a transcription factor that transcriptionally activates downstream target genes involved in cell cycle arrest, senescence and apoptosis such as *CDKN1A* ($p21^{WAF1}$), *PUMA*, *FAS,* and *TP53INP1* [17–21]. P53 can also inhibit cell growth by transcriptionally activating SESTRIN (SESN) family genes such as *SESN2*, which are known negative regulators of the mTORC1 complex [22,23]. The importance of p53 in tumor suppression is further supported by the findings that the *TP53* gene is inactivated due to genomic alterations such as gene mutation and/or deletion in approximately 50% of all human cancers including advanced prostate cancer (PCa) [24–27]. The tumor suppressor function of p53 is also regulated by protein posttranslational modifications including acetylation and methylation [28,29]. However, major pathways that influence p53 tumor suppression signaling networks beyond *TP53* gene/protein itself remain elusive.

PCa is the most-commonly-diagnosed cancer among men in the United States and other Western countries. Androgen deprivation therapy (ADT) is the mainstay treatment for most advanced PCa because of their dependency on androgen/androgen receptor (AR) signaling for growth and survival [30,31]. However, the majority of these tumors relapse after ADT and become castration-resistant prostate cancer (CRPC), which is usually treated with the second-generation antiandrogens such as enzalutamide (ENZ) or the first-line chemotherapy

taxane (e.g. docetaxel (DTX)) [32–35]. In addition to blocking the depolymerization of microtubules, we and others have shown that DTX also enables to inhibit AR activities in CRPC cells through various mechanisms [36–39]. Since CRPC patients often progress on the treatment of ENZ or taxane in clinic, it is important to unfold the molecular mechanisms underlying therapy resistance and identify new therapeutic targets for CRPC.

Herein, we demonstrate that *FTO* intronic transcript 1 (*FTO-IT1*) is upregulated in therapy-resistant PCa. We further show that *FTO-IT1* acts as a suppressor of the m^{6}A MTase 'writer' complex and p53 tumor suppression signaling by binding to RBM15 and diminishing mRNA m^{6}A methylation and stability of a subset of p53 target genes, thereby phenocopying p53 genomic alteration or functional inactivation.

Results

FTO-IT1 is upregulated during PCa progression and negatively correlated with patient survival

To elucidate the molecular mechanisms of antiandrogen therapy resistance in PCa, we performed transcriptomic analysis in control and ENZ-resistant C4–2 cell lines (hereafter termed C4–2C and C4–2R, respectively) we generated previously [40,41]. Since drug resistance mechanisms mediated by coding RNAs and protein posttranslational modifications have been extensively studied in PCa [42,43], we chose to focus on ncRNAs and RNA posttranscriptional modifications such as m^{6}A. Among the 11 known m^{6}A 'writer' and 'reader' genes, we found that ncRNAs are expressed at or near three of these gene loci and *FTO-IT1*, a long ncRNA (lncRNA) transcribed from intron 8 of *FTO* gene, was significantly upregulated in C4–2R compared to C4–2C cells (Figures 1A, 1B and S1A and Tables S1-S3). *FTO* mRNA was also elevated in C4–2R cells compared to C4–2C cells (Figure S1B). RNA fluorescent in situ hybridization (RNA-FISH) analysis showed that *FTO-IT1* was localized in both the cytoplasm and nucleus of C4–2 cells and that ENZ treatment induced *FTO-IT1* expression but had no obvious effect on *FTO-IT1* cellular distribution (Figures 1C, 1D and S1C). RNA copy number analysis showed that *FTO-IT1* levels were lower in C4–2C cells but much higher in C4–2R and 22Rv1, another ENZ-resistant cell line [44] (Figure S1D).

We demonstrated that synthetic androgen mibolerone induced, but ENZ inhibited AR binding in a putative enhancer (H3K4me- and H3K27ac-positive) in the *FTO-IT1* locus in C4–2 cells (Figure S1E and S1F). Androgen deprivation or treatment with ENZ or AR proteolysis-targeting chimera (PROTAC) ARV-110 [45] increased, but AR overexpression repressed *FTO-IT1* expression in C4–2 cells (Figure S1G-S1I). DTX is known to suppress AR function [36–39] and we demonstrated that the expression level of *FTO-IT1*, but not *FTO* was higher in DTX-resistant 22Rv1, C4–2, and LNCaP cells compared to control cells (Figures 1E and S2A). Thus, *FTO-IT1* lncRNA is a repression target of the AR and ENZ and DTX promote *FTO-IT1* de-repression and overexpression in PCa cells.

Meta-analysis of transcriptomic data in primary PCa samples from The Cancer Genome Atlas (TCGA) cohort showed that *FTO-IT1* expression was higher in tumors in advanced-stages (T3b and T4) relative to early-stages (T2a to T3a) (Figure 1F). *FTO-IT1* RNA was

significantly upregulated in metastatic CRPC tissues compared to primary tumors (Figure 1G). In contrast, *FTO* mRNA was not elevated in advanced stages or CRPC samples (Figures S2B and S2C). Knockout of *FTO-IT1* by CRISPR/Cas9 re-sensitized C4–2R cells to ENZ but had no obvious effect on ENZ sensitivity in C4–2C cells (Figure S2D-S2G). In contrast, *FTO* knockdown did not alter ENZ sensitivity in C4–2C and C4–2R cells (Figure S2H).

High *FTO-IT1* expression significantly associated with poor progression-free survival (PFS) of PCa patients in the TCGA cohort, but no such effect in metastatic PCa patients of the West Coast Dream Team (WCDT) cohort (Figures S2I and S2J). By stratifying tumors with alterations often occurred in PCa such as *AR* amplification, *TMPRSS2-ERG* fusion and *TP53* gene deletion/mutation, we found that high levels of *FTO-IT1* significantly associated with worse PFS in TCGA and worse overall survival of patients in WCDT (Figures 1H and 1I). However, there was no such association with *FTO* mRNA expression in both cohorts (Figures S2K and S2L). These data indicate that high *FTO-IT1* expression associates with poor disease progression only in patients with prostate cancers harboring WT *TP53*, implying a functional tie between *FTO-IT1* overexpression and p53 signaling.

FTO-IT1 downregulates m^{6}A levels on a subset of p53 target gene mRNAs

Next, we examined the effect of *FTO-IT1* on mRNA m^{6}A levels due to its expression from the *FTO* gene locus. Both dot blot and mass spectrometry analyses showed that *FTO-IT1* KO substantially increased global mRNA m^{6}A levels in C4–2R and 22Rv1 cell lines (Figures 2A, S2M and S2N). The effect of *FTO-IT1* KO on m^{6}A$_m$, a modification occurred at the cap of mRNAs [46] was very minimal in both C4–2R and 22Rv1 cells (Figure S2O) and not pursued further.

By performing bulk RNA-seq and m^{6}A-methylated mRNA immunoprecipitation sequencing (MeRIP-seq), we identified a total of 10,038 and 14,739 m^{6}A peaks overlapped in two replicates in mock and *FTO-IT1* KO cells, respectively (Tables S4-S6). The confidence on these peaks was further evident by merging the peaks from two replicates (Tables S7 and S8). Similarly, a large number of individual m^{6}A peaks (n = 3,201) were up- but a much smaller number of peaks (n = 573) were down-regulated in *FTO-IT1* KO 22Rv1 cells compared to control cells (Figure 2B and Table S9). Relative to control cells, *FTO-IT1* KO cells exhibited m^{6}A increase primarily in coding sequence (CDS) and parts of 3'UTR (Figure 2C and Tables S6 and S9). Consistent with previous reports [47,48], the m^{6}A frequency reaches its peak near the stop codon, but the peak was higher in *FTO-IT1* KO cells compared to control cells (Figure 2C). These findings reveal a role of *FTO-IT1* in inhibiting the overall mRNA m^{6}A levels in cells.

Bulk RNA-seq revealed 1,229 up- and 1,777 down-regulated genes in *FTO-IT1* KO versus control 22Rv1 cells (Figure 2D and Table S10). Pathway analysis indicated the upregulated genes were enriched in a few pathways such as p53 transcriptional gene networks while the downregulated genes were enriched in other pathways such as PLK1 and AURORA B signaling (Figures S3A and S3B). Clustering analysis revealed 1,226 hypermethylated peaks from 649 upregulated genes (hyper-up) but only 253 hypermethylated peaks from 188 down-regulated genes (hyper-down) (Figure 2E and Table S11). This result indicates that

m^{6}A hypermethylation associates with more upregulated genes in 22Rv1 cells, prompting us to focus on *FTO-IT1* regulation of hyper-up genes.

Similar to the hypermethylated targets, p53 transcriptional target genes were also among the top hyper-upregulated genes induced by depletion of *FTO-IT1* (Figure 2F). Considering that high level *FTO-IT1* expression only significantly associated with poor survival of p53 WT PCa patients (Figures 1H and 1I), we chose to focus on *FTO-IT1* regulation of the p53 pathway genes. Gene Set Enrichment Analysis (GSEA) further confirmed the enrichment of p53 pathway as a hallmark change in *FTO-IT1* KO cells (Figure S3C). Indeed, a group (n = 36) of p53 pathway genes including those defined by GSEA such as *FAS*, *TP53INP1*, *SESN2* and *MDM2* were significantly upregulated in *FTO-IT1* KO cells relative to control cells (Figures 2G–2I, S3D and S3E). These results were further confirmed by MeRIP-qPCR (Figure 2J). *FTO-IT1* knockout increased the stability of these mRNAs and their expression at both mRNA and protein levels (Figures 2K, 2L, S3F and S3G). *FTO-IT1* KO modestly decreased the steady state level and half-life of p53 protein in both 22Rv1 and C4–2R cells, which is consistent with the modest increase in MDM2, a known E3 ubiquitin ligase targeting p53 protein for degradation (Figures 2L and S3F-S3I). *FTO-IT1* KO only had very minimal effect on p53 pathway genes in C4–2C control cells (Figure S3J). On the contrary, *FTO-IT1* overexpression decreased p53 target gene mRNA m^{6}A level and their stability in 22Rv1 cells (Figures S3K-S3M). Similar results were observed in C4–2R (*FTO-IT1* high) compared to C4–2C (*FTO-IT1* low) cells (Figures S3N and S3O).

P53 signaling is known to be activated in response to DNA damage. We constructed a sgRNA targeting a gene desert region and demonstrated that DNA cut mediated by CRISPR/Cas9 in this gene desert region did not activate p53 pathway genes (Figures S3P-S3R). We also surveyed *FTO-IT1* expression in a large panel of breast cancer cell lines (Table S12). *FTO-IT1* expression was higher in MDA-MB-468 cells compared to most of the other cell lines (Figure S3S). *FTO-IT1* KO increased overall mRNA m^{6}A levels and p53 gene mRNA expression in MDA-MB-468 cells (Figures S3T and S3U), suggesting that *FTO-IT1* regulation of p53 signaling may occur in other cancer types. Together, increased expression of *FTO-IT1* decreases mRNA m^{6}A levels and stability of a subset of p53 target genes related to cell cycle and apoptosis.

FTO-IT1 regulates cell growth and survival via m^{6}A-mediated p53 target gene expression

Colony formation assays showed that *FTO-IT* KO 22Rv1 and C4–2R cells grew much slower than control cells (Figures 3A and 3B). *FTO-IT1* knockout induced G1 cell cycle arrest in 22Rv1 cells (Figures 3C, 3D, S4A and S4B). The SESTRIN (SESN) family proteins play important roles in suppression of mTORC1 and mTORC2, activation of which induces upregulation of cell cycle drivers and downregulation of cell cycle inhibitors [22]. Consistent with the upregulation of *SESN2*, a known p53 target gene [22,49] and the downregulation of phosphorylation of S6K, a downstream effector of mTORC1 in *FTO-IT1* deficient cells (Figures 2G and 2L), depletion of *SESN2* abolished *FTO-IT1* KO-induced cell cycle arrest (Figures 3E–3G), suggesting an important role of SESN2 in mediating *FTO-IT1* regulation of the cell cycle. *FAS* and *TP53INP1* are two known p53 target genes that promote apoptosis [20,50]. *FTO-IT1* depletion induced apoptotic cell death (Figures

3H, 3I, S4C and S4D), and knockout of *FAS* or *TP53INP1* individually partially blunted *FTO-IT1* KO-induced apoptosis in 22Rv1 cells (Figures 3J–3O). The effects of *FTO-IT1* on cell cycle and apoptosis remained significant even when cells were treated with the DNA damaging agent camptothecin (CPT) although CPT treatment did increase basal level of G1 cell cycle arrest and apoptosis as expected (Figures S4E-S4I). However, *TP53* knockout almost completely abolished *FTO-IT1* KO-induced cell cycle arrest and apoptosis (Figures S4J-S4N). Expression level but not mRNA m^6A level (after normalized with input) of *CDKN1A* (encodes $p21^{WAF1}$), another well-recognized p53 target gene was also upregulated in *FTO-IT1* KO cells (Figures 2G and S4O). Knockdown of *CDKN1A* partially attenuated *FTO-IT1* KO-induced cell cycle arrest (Figures S4P-S4R), suggesting a role of *FTO-IT1* in regulating p53 target gene expression and cell cycle progression in both mRNA m^6A modification-dependent and independent manners.

FTO-IT1 directly binds with RBM15

Knockout of *FTO-IT1* modestly decreased *FTO* mRNA expression in 22Rv1 and C4–2R cells, but the changes were even more subtle at the protein level (Figures S5A-S5C). The discrepancy in the mRNA and protein levels could be due to the very long turnover time of FTO protein in both 22Rv1 and C4–2R cells (Figures S5D and S5E), consistent with a previous report in other cancer types [51]. In contrast, *FTO-IT1* KO had little or no effect on FTO expression in LAPC4 and PC-3 PCa cell lines (Figures S5F and S5G). *FTO-IT1* deletion had no obvious impact on the expression of other m^6A modifiers examined in both 22Rv1 and C4–2R cell lines (Figure S5C).

Since *FTO-IT1* manipulation did not drastically affect the expression levels of the m^6A writers and erasers, we sought to determine whether *FTO-IT1* binds to these proteins. RNA pulldown and mass spectrometry analysis showed that *FTO-IT1* uniquely bound to a total of 280 proteins (Table S13), among which RBM15 was the only m^6A modifier protein (Figures 4A–4D). Western blot analysis confirmed that *FTO-IT1* interacted strongly with RBM15, weakly with RBM15B, METTL3, METTL14 and WTAP but had no obvious association with other members of the ‘writer’ complex (Figure 4E). *In vitro* protein pulldown assays showed that *FTO-IT1* directly bound to RBM15, but not METTL3, METTL14 and WTAP (Figures 4F–4I). CLIP-qPCR assay showed that RBM15 bound to the 3’-stem-loop region of *FTO-IT1* (SL3) (Figures 4J and 4K). Reciprocally, RNA pulldown using full-length and SL3-truncated *FTO-IT1* RNA confirmed that SL3 is essential for RBM15 binding (Figure 4L). RIP with GST and GST-RBM15 recombinant proteins and *in vitro* transcribed *FTO-IT1* showed that *FTO-IT1* directly binds the RRM1 domain of RBM15 (Figures 4M and 4N).

RBM15 selectively binds and increases m^6A levels of a subset p53 target gene mRNAs

RBM15 is an RNA-binding-motif-containing protein that is reported to bind a large number of RNAs and facilitates RNA m^6A methylation [5]. By performing RBM15 CLIP-seq in 22Rv1 cells, we demonstrated that the RBM15 binding sites were highly aligned with m^6A sites enriched by the GAC motif and peaked at or near the stop codon (Figures S6A-S6C). The 3,498 RBM15-bound mRNAs identified by CLIP-seq significantly overlapped with the well-established p53 pathway genes (Figure 5A and Tables S14-S16), Among the 68 overlapped p53 targets, 49 mRNAs were m^6A methylated (Table S17) and 13 of them

were hypermethylated upon *FTO-IT1* KO, including *FAS*, *TP53INP1*, *SESN2*, and *MDM2* (Table S17). CLIP-seq and m^{6}A IP data displayed a significant consistency between RBM15 binding sites and m^{6}A peak sites in the body of *FAS*, *TP53INP1*, *SESN2*, and *MDM2* genes (Figure 5B). CLIP-qPCR confirmed that *FTO-IT1* KO and overexpression (OE) increased and decreased RBM15 binding of these p53 target gene mRNAs, respectively but had mixed effects on other p53 targets (e.g. *JUN, LDHB* and *NOTCH1*) and no effect on the *FTO-IT1*-unaffected RBM15 binding target *MYC* and the RBM15-unbound target *HPRT1* (Figures 5C, 5D and S6D). *RBM15* knockdown not only decreased the basal m^{6}A levels on these p53 target gene mRNAs and their expression, but also abolished *FTO-IT1* KO-induced increase in m^{6}A methylation and expression of these mRNAs (Figures 5E–5J). Given that RBM15 is a key component of the m^{6}A 'writer' complex that regulates RNA m^{6}A methylation [5], we sought to determine the role of the m^{6}A MTase complex in *FTO-IT1* regulation of m^{6}A levels on p53 target gene mRNAs. Similar results were obtained by knockdown of METTL3, a catalytic subunit of the MTase complex (Figures S7A-S7C). These data indicate that the effect of *FTO-IT1* on p53 target gene mRNA m^{6}A modification and expression is primarily mediated through the MTase writer complex.

RBM15 binds to p53 protein and regulates p53 target mRNA m^{6}A level and expression

Previous studies indicate that m^{6}A is co-transcriptionally deposited on mRNAs [1]. To investigate how RBM15 regulates p53 target gene mRNA m^{6}A level, we performed meta-analysis of p53-interacting proteins identified by mass spectrometry in the BioGRID database and found that RBM15 was the only one of the m^{6}A modifiers bound by p53 (Figure 6A). We demonstrated that at endogenous level p53 interacted strongly with RBM15, marginally with METTL3, but not other core components of the m^{6}A writer complex including METTL14 and WTAP and RBM15B (Figure 6B). Reciprocal co-IP confirmed this result (Figure 6C). In addition, knockout of *FTO-IT1* did not affect RBM15 and p53 protein cellular localization and RBM15 interaction with p53 and other MTase complex components examined (Figures S7D-S7F). GST pulldown assay using GST-RBM15 recombinant proteins and *in vitro* transcribed and translated p53 proteins showed that the SPOC domain in the C-terminal end of RBM15 directly bound p53 protein (Figures 6D and 6E). Reciprocally, we showed that p53 DNA binding domain (DBD) was required for RBM15 interaction (Figures 6F and 6G). RBM15 ChIP-qPCR analysis revealed the binding of RBM15 in these p53 target gene loci, but the binding was largely diminished by *TP53* KO (Figures 6H and 6I). Co-IP assay demonstrated that deletion of the SPOC domain abolished RBM15 binding of p53 (Figures S7G and S7H). We further showed that restored expression of WT RBM15, but not the RBM15ΔSPOC mutant increased m^{6}A levels and expression of p53 target mRNAs (Figures 6J–6L), highlighting the importance of RBM15 in regulating p53 target gene mRNA m^{6}A levels. The defect of RBM15ΔSPOC in regulating p53 target mRNA m^{6}A and expression can be alternatively explained by the inability of this mutant to interact with the MTase complex (Figure S7H), consistent with a previous report [52]. Collectively, these data indicate that RBM15 directly binds p53 protein and regulates p53 target gene mRNA m^{6}A modification and expression.

IGF2BP proteins bind and stabilize m^{6}A-modified p53 target gene mRNAs

The fate of m^{6}A-methylated RNAs can be either up- or down-regulated due to their recognition by different m^{6}A 'reader' proteins including YTHDC1–2 and YTDHF1–3) [53–59] and IGF2BP1–3 [53]. IGF2BP proteins can regulate the stability of m^{6}A-methylated RNAs [53]. Because our data show that *FTO-IT1* negatively regulates the m^{6}A level and stability of p53 target gene mRNA, we sought to determine whether IGF2BP proteins play a role in *FTO-IT1* regulation of p53 gene mRNA expression. We found that IGF2BP1–3 bound p53 target gene mRNAs and that *FTO-IT1* KO largely enhanced their binding of p53 targets but not *MYC* mRNA, a known IGF2BP recognition target [53] (Figures S7I-S7K). Knockout of *IGF2BP1–3* decreased p53 target gene expression and almost completely blocked *FTO-IT1* KO-induced upregulation of these genes (Figures S7L and S7M). *FTO-IT1* KO failed to increase the stability of these gene mRNAs in *IGF2BP1–3*-depleted cells (Figure S7N). Similarly, *FTO-IT1* KO-induced G1 cell cycle arrest and apoptosis were completely reversed by *IGF2BP1–3* KO in 22Rv1 cells (Figures S7O-S7R), highlighting a pivotal role of IGF2BP proteins in mediating *FTO-IT1* regulation of p53 target gene mRNA stability and inhibition of PCa cell growth.

FTO-IT1 depletion inhibits PCa cell growth *in vitro* and in mice

We demonstrated that *FTO-IT1* KO largely inhibited C4–2R tumor growth *in vivo* (Figures 7A–7C). Immunohistochemistry (IHC) showed that *FTO-IT1* KO decreased proliferation and increased apoptosis in these tumors (Figures S8A and S8B). We designed *FTO-IT1*-specific antisense oligonucleotides (ASOs) and identified two most potent ones (#3 and #6) that yielded > 80% of reduction in *FTO-IT1* expression (Figure 7D). Administration of these two *FTO-IT1* ASOs largely increased p53 target gene expression in 22Rv1 and C4–2R cells (Figure 7E). ASO treatment largely increased cleaved PARP1 level, decreased RB phosphorylation and significantly inhibited cell proliferation and colony formation ability (Figures 7E–7G, S8C and S8D). *FTO-IT1* ASOs also increased global mRNA m^{6}A levels in both C4–2R and 22Rv1 cells (Figure S8E). *FTO-IT1* ASO administration largely inhibited tumor growth but not mouse body weight (Figures 7H–7K). The ASO treatment also increased global m^{6}A abundance, p53 target gene mRNA m^{6}A level and expression, inhibited cell proliferation and induced apoptotic cell death in tumors (Figures 7L, 7M and S8F-S8H). These data indicate that overexpressed *FTO-IT1* is a viable therapeutic target of cancer.

Discussion

The *FTO* gene locus appears to be a functionally dynamic, but not fully appreciated genomic region. FTO affects a large spectrum of biological processes by acting as a RNA m^{6}A demethylase [1,7]. FTO also controls mTORC1 activities and amino acid sensing independently of the demethylase function [13]. Additionally, enhancer activity in intron 1 of the *FTO* gene has been linked to obesity-associated SNPs (genomic variants) to the role of *IRX3* expression in obesity [11]. In the present study we observed that *FTO-IT1*, a lncRNA transcribed from the last intron of the *FTO* gene is overexpressed during PCa progression and overexpressed *FTO-IT1* induces downregulation of global and p53 target gene mRNA m^{6}A levels in PCa cells by binding to and intervening the activities of the

m^{6}A methyltransferase complex. Thus, our study identifies a previously uncharacterized noncoding RNA as another key functional element in the *FTO* gene locus that restrains mRNA m^{6}A modification and expression of p53 target gene such as *SESN2*, a key negative regulator of mTORC1 [22,23] and p53 tumor suppression function (Figure 8).

It is well known that the tumor suppressor function of p53 is often inactivated by genetic alterations (gene mutation and/or deletion) or aberrant protein degradation [25,60]. We demonstrate that with no effect on *TP53* gene mRNA and only marginal effect on p53 protein expression *FTO-IT1* inhibits p53 tumor suppression signaling by largely decreasing the mRNA m^{6}A levels of a few key p53 downstream target genes. Notably, depletion of each of these genes only partially reverses the activation of p53 tumor suppression function induced by *FTO-IT1* KO, further supporting the notion that individual p53 target genes do not account for all of p53 function [61,62]. We further show that RBM15 directly binds to p53 protein and induces p53 target gene mRNA m^{6}A methylation, thereby revealing a new connection of the m^{6}A MTase 'writer' complex to p53 signaling, a mechanism in parallel to the direct binding of p53 by METTL3 reported recently [63] (Figure 8, Top). However, this effect of RBM15 was abolished by *FTO-IT1* binding of RBM15 (Figure 8, Bottom). Thus, our study identifies *FTO-IT1* as a *bona fide* suppressor of the MTase 'writer' complex, a pivotal mechanism in suppression of mRNA methylation complementary to the exon junction complex discovered recently [64]. Our findings also reveal a previously unrecognized epitranscriptomic mechanism that circumvents the tumor suppressor activity of WT p53 by disrupting its downstream target gene signaling beyond *TP53* gene itself, thereby phenocopying genomic inactivation of *TP53* gene.

A previous study shows that RBM15 mainly binds to the U-rich motifs in the 3'-UTR of target genes in 293T cells (Patil et al., 2016). We found that RBM15 mainly bound to the CDS of genes with binding peaks at stop codon (similar to the m^{6}A distribution) in PCa cells and "GACG" was the most enriched motif although a small percentage of U-rich motifs was also observed. This "inconsistency" is possibly due to different cell contexts given that different cell models were used in these studies. This phenomenon further supports the notion that the role of m^{6}A modifiers is cell context-dependent. While the current study was ongoing, METTL3 was identified most recently by an independent group as a p53-interacting partner under genotoxic stress conditions [63,65]. Based on these studies, we envisage a model whereby p53 associates with the MTase 'writer' complex via directly interacting with RBM15 and/or METTL3 in the presence or absence of extracellular stress stimuli (Figure 8, Top).

Consistent with the recent report [63,65], our data reveal that there is a m^{6}A methyltransferase complex-augmented tumor suppressor action of p53 (Figure 8, Top). However, this role of the MTase complex appears to be conditional and it can be intrinsically impaired by *FTO-IT1* lncRNA overexpression (Figure 8, Bottom). Importantly, due to the reversible nature of m^{6}A modification [1,66], we provide evidence that *FTO-IT1* overexpression-induced inhibition of p53 target gene mRNA m^{6}A modification, inactivation of p53 target gene networks and augmented tumor growth can be abolished by therapeutic targeting of *FTO-IT1*. We show that depletion of *FTO-IT1* by ASOs not only restores the expression of p53 target genes, but also largely inhibits PCa cell growth *in vitro* and in mice. Thus, our

findings stress that overexpressed *FTO-IT1* could be a viable biomarker and therapeutic target of tumors, especially those p53-WT cases where mRNA m^6A methylation-dependent p53 tumor suppression networks are inactivated by overexpressed *FTO-IT1*.

Limitations of the Study.

Our transcriptomic analysis shows that a group of p53 target genes are upregulated upon *FTO-IT1* knockout; however, only a subset of them are affected by m^6A modification. It is possible that *FTO-IT1* may also regulate p53 tumor suppression signaling via the mechanism(s) independent of m^6A methylation, which are unclear at present. While we show that *FTO-IT1* directly binds to RBM15 and inhibits its effect on mRNA m^6A modification, we noticed that not all RBM15-bound m^6A-modified p53 target gene mRNAs are affected by *FTO-IT1*. The exact underlying mechanism remains to be determined.

STAR Methods

Resource availability

Lead Contact—Further information and requests for resources and reagents should be directed to and will be fulfilled by the Lead Contact, Haojie Huang (Huang.Haojie@mayo.edu).

Materials Availability—All unique/stable reagents generated in this study are available from the Lead Contact with a completed Materials Transfer Agreement.

Data and Code Availability—All sequencing data generated in this study have been deposited in NCBI Gene Expression Omnibus (GEO): GSE189966, GSE189465, GSE212043, GSE229871. The mass spectrometry proteomics data have been deposited to the ProteomeXchange Consortium via the PRIDE partner repository with the dataset identifier PXD041053 and 10.6019/PXD041053. Raw images of gels have been deposited at Mendeley Data. All data are publicly available as of the date of publication. Accession numbers and DOI are listed in the key resources table.

This paper does not report original code.

Any additional information required to reanalyze the data reported in this paper is available from the Lead Contact upon request.

Experimental Model and Study Participant Details—22Rv1, LNCaP, PC-3, LAPC4, MDA-MB-468 and 293T cells were obtained from the American Type Culture Collection (ATCC). C4–2 cells were purchased from Uro Corporation. 22Rv1, C4–2, LNCaP and PC-3 cells were maintained in RPMI1640 supplemented with 10% FBS. 293T and LAPC4 cells were maintained in DMEM supplemented with 10% FBS. MDA-MB-468 cells were maintained in Leibovitz's L15 supplemented with 10% FBS. C4–2R cells were generated by treating C4–2 cells with 10 μM enzalutamide for one month.

Method details

Antibodies and reagents—The antibodies used in this study are listed in key resources table.

Plasmids—GST-tagged RBM15 and Myc-tagged RBM15 were generated by cloning the corresponding cDNA into the pGEX-4T-1 and pCMV vector, respectively. HA-tagged p53 plasmids were previously generated in our lab. *FTO-IT1* expression plasmid was generated by cloning the cDNA into the pCDNA-3.1 vector. The cDNA fragments were amplified by Phusion polymerase (NEB) using Phusion High-Fidelity PCR Master Mix. The primers used for plasmid construction and knock out test are listed in Table S18.

Transfection, and lentivirus infection—For transient transfection, cells were transfected with Lipofectamine 2000 (Thermo Fisher) according to the manufacturer's instructions. For lentivirus production, the pLenti-CRISPR-V2 plasmid containing corresponding sgRNA sequence or pLKO-based gene shRNA knockdown plasmids or pTsin plasmid containing corresponding gene CDS were mixed with pMD2.G and psPAX2 and transfected into 293T cells. The virus-containing supernatant was harvested 48 h after transfection to infect PCa cells in the presence of 10 μg/ml polybrene. The successfully infected cells were selected with 1 μg/ml puromycin. The shRNA plasmids were purchased from Sigma-Aldrich. The shRNA/siRNA sequences targeting *METTL3*, *SESN2* and *RBM15*, and the sgRNA sequences targeting *FTO-IT1*, *IGF2BP1, IGF2BP2, IGF2BP3, FAS, TP53INP1* are listed in Table S19.

Generation of knockout cell lines—We generated coding gene knockout cell lines using the CRISPR/Cas9 approach as previously described [67]. To knock out a noncoding RNA or a genomic region in a gene desert region, in each case we designed a pair of sgRNAs targeting each end of the designated genomic region. The cells were co-infected with lentivirus for CRISPR/Cas9 and sgRNAs and selected with puromycin. The genomic DNA was isolated from stable clones for PCR amplification. Knockout of *FTO-IT1* was also confirmed by RT-qPCR at the RNA level.

Antisense oligonucleotides (ASOs) design and screening—ASOs were designed based on the complementary sequence of *FTO-IT1* with phosphorothioate (PS) backbone and MOE modification on the flanking six nucleotides (IDT). ASOs were transfected into 22Rv1 cells followed by RT-qPCR analysis and the highly efficient ASOs were used for further studies. ASO sequences are listed in Table S19.

RNA isolation from human prostate cancer specimens—Formalin-fixed paraffin-embedded (FFPE) hormone-naïve primary PCa and CRPC tissues were randomly selected from the Mayo Tissue Registry. RNAs were isolated using a RecoverAll Total Nucleic Acid Isolation Kit (Invitrogen). Informed consent was obtained from all human participants, and the studies were approved by the Institute Review Board (IRB) of the Mayo Clinic.

***FTO-IT1* RNA copy number measurement—**RNA copy number measurement was performed as previously described [41]. Briefly, *FTO-IT1* was cloned

into the pcDNA3.1 backbone vector. The cDNA copy number and dilution calculation were performed using the method described in the web site shown below. (https://www.lifetechnologies.com/us/en/home/brands/thermo-scientific/molecular-biology/molecularbiology-learning-center/molecular-biology-resource-library/thermo-scientific-web-tools/dna-copy-numbercalculator.html.) 1×10^5 cells were used for RNA extraction and the total RNA was diluted in 100 μl H_2O. One microliter of RNA was used for reverse transcription and 1% of the cDNA was used for qPCR. The final Ct value correspond to the copy number in 10 cells. A standard curve was used to correspond the Ct value with actual copy number. Copy number was calculated by the equation derived from standard curve.

RNA extraction from cultured cells and reverse transcription-quantitative PCR (RT-qPCR)—The total RNA was isolated using TRIzol reagent (Thermo Fisher Scientific) and reverse-transcribed to cDNA using superscript RT kit (Promega GoScript) according to manufacturer's instruction. Quantitative PCR was performed using SYBR Green Master mix Kit (Bio-Rad) in Bio-Rad CFX manager 3.1. The quantification of indicated genes was normalized to that of endogenous control *GAPDH*. The primers for RT-qPCR are listed in Table S18.

m^{6}A dot blot—Dot blot of m^{6}A was carried out as previously reported [7]. Briefly, mRNA was purified from total RNA using Dynabeads™ mRNA Purification Kit (Thermo Fisher Scientific). The isolated mRNA was first denatured in 95 °C for 3 min and chilling on ice directly. Two-fold serial dilution of the mRNA were spotted on Biodyne B nylon membrane (PALL) and crosslinked by UV Stratalinker. The membrane was blocked by 5% non-fat milk and incubated with anti-m^{6}A antibody (Synaptic Systems 1:2,000) overnight at 4 °C. Horseradish peroxidase (HRP)-conjugated secondary antibody was used to incubate with the membrane and ECL was used to visualize the signal. A copy of spotted membrane was stained with 0.02% methylene blue in 0.3 M sodium acetate (pH 5.2) to ensure that an equal amount of mRNA was loaded.

m^{6}A RNA immunoprecipitation—Purified mRNA was partially digested with 1 unit of RNase T1 for 2 min and incubated with 2 μg of m^{6}A antibody and protein A/G beads in IPP buffer (10 mM Tris pH7.5, 150 mM NaCl, 0.1% NP-40) supplemented with RNase inhibitor in 4 °C overnight. The beads were washed 6 times and the RNA was extracted using TRIzol reagent. RT-qPCR was performed to detect the enrichment of m^{6}A modified RNA.

mRNA m^{6}A and m^{6}Am methylation level measured by LC-MS/MS—LC-QqQ-MS/MS measurements were performed as reported previously [6]. In brief, total RNA was purified with TRIzol® reagents (Thermo Fisher Scientific, #15596018) from fresh cells. mRNA was isolated by using Dynabeads® mRNA DIRECT kit (Thermo Fisher Scientific, #61006) twice. After that, rRNA was further removed using RiboMinus Eukaryote kit (Thermo Fisher Scientific, A1083708). The purified mRNA was further digested into nucleotides with nuclease P1 (Sigma, N8630) in 20 ml of buffer containing 25 mM NaCl and 2.5 mM ZnCl2 for 1 h at 42°C, and then 1 unit of FastAP Thermosensitive Alkaline Phosphatase (1 U/μl, Thermo Fisher Scientific, EF0651) in FastAP buffer for another 4 h at

37°C. Samples were then filtered (0.22 mm, Millipore) and injected into a C18 reverse phase column coupled online to Agilent 6460 LC–MS/MS spectrometer in positive electrospray ionization mode. The nucleosides were quantified by using retention time and the nucleoside to base ion mass transitions (268-to-136 for A; 296-to-150 for m^6Am, and 282-to-150 for m^6A). Quantification was performed by comparing with the standard curve obtained from pure nucleoside standards running with the same batch of samples.

m^6A-seq library preparation and data analysis—mRNA was purified from total RNA by using Dynabeads® mRNA DIRECT kit (Thermo Fisher Scientific, #61006). 1 μg mRNA in 100 ul RNase free water was fragmented to ~200 nt using Bioruptor® Pico Sonication Instrument with 30 cycles of 30s on/30s off mode. 5 μl of the fragmented mRNA was saved as input. The remaining fragmented mRNA was subjected to m^6A IP by using the EpiMark®N6-Methyladenosine Enrichment Kit (NEB, E1610S) following the manufactory protocol. RNA libraries were prepared for both input RNA and m^6A-enriched mRNA after IP using TruSeq® Stranded mRNA Library Prep (Illumina, 20020594) following the manufacturer's protocol. Sequencing was performed at the University of Chicago Genomics Facility on an Illumina HiSeq 2000 machine in single-read mode with 50 bp per reading at around 25 M to 30 M sequencing depth. After obtaining the raw data, single-end reads were harvested and trimmed by Trim_Galore to remove adaptor sequences and low-quality nucleotides. High-quality reads were then aligned to UCSC hg19 reference genome by HISAT2 using default parameters, and only uniquely mapped reads were retained for all downstream analyses. FeatureCounts software was used to count reads mapped to RefSeq genes, and differentially expressed genes analysis was conducted by DESeq 2 Software. m^6A peaks on RefSeq transcripts and differentially methylated m^6A peaks were analyzed by ExomePeak R package. To visualize sequencing signals at specific genomic regions, we used Deeptools to normalize all libraries and imported into IGV.

***In vitro* transcribed biotin-labeled RNA pulldown—**Full-length and fragments of *FTO-IT1* were amplified by PCR using *FTO-IT1* specific primers with the forward primer containing a T7 promoter. Biotin-labeled RNAs were *in vitro* transcribed using corresponding PCR products as template and Biotin RNA Labeling Mix (Roche) and T7 polymerase (New England Biolabs). Control biotin-labeled RNA was *in vitro* transcribed using empty pcDNA3.1-SFB vector as template (~ 600 nt) which contains a T7 promoter and the sequences of V5 epitope, polyhistidine, SFB tags (S tag, Flag tag and biotin binding protein (streptavidin) binding peptide) and some other sequences before the polyadenylation signal. The transcribed RNA products were treated with DNase I to eliminate the template DNA. 22Rv1 cells were lysed in modified binding buffer (50 mM Tris pH7.5, 150 mM NaCl, 1% NP-40, 0.1% SDS) supplemented with protease inhibitor and RNase inhibitor. For *in vitro* translated protein, plasmid containing RBM15 gene sequence and T7 promoter was incubated with TNT Quick Master Mix (PR-L1170) for 90 min. Cell lysates or *in vitro* translated protein were incubated with biotin-labeled RNAs and streptavidin beads at 4 °C for 12 h. The beads were washed with wash buffer (50 mM Tris pH7.4, 150 mM NaCl, 0.05% NP-40, 1mM MgCl2) for 4 times. The samples were resolved in SDS loading buffer and denatured in 95 °C. Western blot and mass spectrometry were used to analyze the interaction proteins. The primers for *FTO-IT1* fragments PCR are listed in Table S18.

In vitro* transcription and RNA pulldown by GST proteins—FTO-IT1* RNA was transcribed *in vitro* using T7 RNA polymerase (New England Biolabs) and NTP Mix (Thermo). The transcribed RNA products were treated with DNase I to eliminate the templated DNA. Plasmids of pGEX-4T-1 containing truncated GST-RBM15 proteins were transformed in *E. coli* (BL21) and induced by 0.1 mM IPTG at 16 °C for 12 h. The GST-RBM15 proteins were purified by glutathione Sepharose beads (GE Healthcare) as previously described (Wang et al., 2013). Purified GST-RBM15 proteins with glutathione Sepharose beads were incubated with *in vitro* transcribed *FTO-IT1* RNA in RNA structure buffer (50 mM Tris pH7.4, 150 mM NaCl, 1 mM MgCl2) at 4 °C for 4 h. After 6 times of wash, the RNAs were purified by Trizol and detected using RT-qPCR.

GST pulldown of ectopically expressed protein and *in vitro* translated protein —Plasmids encoding p53 truncations were transfected into 293T cells. After 36 h, the cells were lysed with IP buffer (50 mM Tris pH7.5, 150 mM NaCl, 0.5% NP-40) and the cell lysates were incubated with purified GST-RBM15 protein as described previously. For *in vitro* translated protein, plasmid containing p53 gene sequence and T7 promoter was incubated with TNT Quick Master Mix (PR-L1170) for 90 min. The *in vitro* translated protein was then incubated with GST-RBM15 protein. After 4 h of incubation and 3 times of wash, the bound proteins were analyzed by Western blot.

RNA fluorescent in situ hybridization (FISH)—RNA FISH was performed as previously described [68]. Briefly, C4–2 cells were seeded on coverslips in 6 well plates. After the cells adhered on the coverslips, 4% paraformaldehyde in PBS was used to fix the cells for 15 min at RT. The fixing solution was removed, and samples were washed twice with PBS. Then 0.5% Triton X-100 in PBS at room temperature for 10 min was applied to permeabilize the cells. After washing with PBS for 3 times, the samples were rinsed with 2 × SSC (0.3 M NaCl, 0.03 M Na3 Citrate, pH 7.0) and hybridization was performed by incubating the samples with 10 nM of FAM-labeled control (antisense) and *FTO-IT1* specific probe mix in hybridization solution (50% Formamide, 2 × SSC, 10% dextran sulfate, 1 mg/ml yeast t-RNA) in a humid box at 37 °C for 16 h. The samples were washed with 2 × SSC for 3 times and 1 × SSC for 3 times and mounted with VECTASHIELD mounting medium. Images were acquired using Zeiss LSM 780 confocal microscope. The intensity of fluorescence signals was quantified and normalized to DAPI using ImageJ. The sequences of probes used in FISH are listed in Table S19.

Cross-linking immunoprecipitation (CLIP)—6 × 150-mm dishes of 22Rv1 cells with 80% confluence were crosslinked by UV254 and harvested. The cells were then lysed in lysis buffer (150 mM NaCl, 0.5% NP-40, 50 mM Tris-HCl (pH 7.5), 2 mM EDTA) with complete, Mini, EDTA-free Protease Inhibitor Cocktail and SUPERNase in at 4°C for 1 hour. Subsequently, the lysis mixture was centrifuged at 17,000 g at 4°C for 30 min and the supernatant was carefully collected. The samples were then treated with RNase T1 (1 u/uL) at RT for 15 min and centrifuged to collect the supernatant, 10% of which was saved as input. Then RBM15 antibody conjugated protein G beads prepared by incubating antibody and beads at 4°C for 6 hours were added into the samples and incubate overnight. For CLIP-qPCR, the beads were washed for 4 times and subjected for Proteinase K de-crosslinking

and RNA extraction. RT-qPCR was used to detect the interaction regions. For CLIP-seq, after washing beads three times, 10 U/μl RNase T1 was added and incubated at RT for 8 min. The beads were then resuspended in 50 μl of SDS-PAGE loading buffer and heated at 95°C for 5 min. The RNA was finally extracted by cutting and recovering the band of RBM15-RNA complex from the SDS-PAGE gel. The libraries for both input and IP samples are prepared using NEBNext® Multiplex Small RNA Library Prep Set for Illumina® (NEB, E7300S). CLIP samples were pooled and sequenced with NovaSeq6000. Raw reads from CLIP samples were first trimmed according to recommended settings [69]. Gene structure annotations were downloaded from UCSC hg19 RefSeq/Repeatmasker. For analysis of CLIP-seq data, we used omniCLIP [70] for peak calling.

RNA stability assay—Cells were treated with 5 μg/ml Actinomycin D and collected at indicated time points. The total RNA was extracted, and mRNA level of each gene was analyzed by RT-qPCR. Linear regression was used to determine the trend line equation based on the changes of mRNA level at different time points. The half-life of each mRNA was calculated through the equation:

$$dC/dt = -K_{decay}\, C$$

Thus, the mRNA degradation rate K_{decay} was estimated by:

$$\ln(C/C_0) = -K_{decay}\, t$$

To calculate the mRNA half-life ($t_{1/2}$), when 50% of the mRNA is decayed (that is, $C/C_0 = 1/2$), the equation was:

$$\ln(1/2) = -K_{decay}\, t1/2$$

From where:

$$t1/2 = \ln 2/K_{decay}$$

Chromatin immunoprecipitation (ChIP) and ChIP-qPCR—For H3K27ac and H3K4me1 ChIP-seq, VCaP cells were fixed with formaldehyde and subjected to sonication by Bioruptor (Diagenode) as described previously [71]. The supernatant was obtained and mixed with protein A/G beads and antibodies for H3K27ac and H3K4me1. After incubation overnight, beads were washed, and the complex containing DNA was eluted at 65°C. The elution was further treated with RNAase and proteinase K. Enriched DNA was extracted for high throughput sequencing. Sequencing libraries were prepared as previously described [72]. The high-throughput sequencing was performed by Illumina HiSeq 4000 platform by the Mayo Clinic Genome Core Facilities. The raw reads were mapped to the human reference genome (GRCh37/hg38) using bowtie2 (version 2.2.9). MACS2 (version 2.1.1) was used for peak calling with a p value threshold of 1×10^{-5} as described [73]. BigWig files were generated for visualization using the UCSC Genome Browser. The assignment of peaks to

potential target genes was performed by the Genomic Regions Enrichment of Annotations Tool (GREAT).

For ChIP-qPCR assays, 22Rv1 cells cultured in 2 × 150 mm dishes were cross-linked for 15 min at room temperature by adding 11% formaldehyde/PBS solution in cell culture medium. Cross-linked cells were scraped into tubes and sonicated with Bioruptor® Pico Sonication Instrument with 10 cycles of 30s on/30s off mode. After centrifugation, the supernatant was incubated with antibody bound protein A/G agarose beads overnight at 4 °C. The beads were washed 4 times. The precipitated protein-DNA complexes were eluted and cross-linking was reversed at 65 °C for 12 h. After Proteinase K digestion, the chromatin was isolated and subjected to qPCR analysis.

Cell cycle analysis—1×10^6 of 22Rv1 cells were suspended by trypsinization and washed with cold PBS. The suspended cells were fixed with 50% cold ethanol and kept in −20 °C overnight. After washing with cold PBS, the fixed cells were resuspended with 0.5 ml PBS and added with 0.2 mg/ml RNase A and incubated for 1 h at 37 °C. The cell suspension was added with 10 μg/ml PI (Sigma P4170) and analyzed on FACS by reading on cytometer at 488 nm. For 2-dimensional FACS, cells were treated with 30 μM BrdU for 30 min before harvested, and fixed with 70% cold ethanol and kept in −20 °C overnight. The cells were then treated with 2 N HCl for 30 min and incubated with BrdU antibody for 30 min followed by FITC labeled secondary antibody for another 30 min. The samples were treated with RNaseA and added with 10 μg/ml PI (Sigma P4170) and analyzed on FACS. The data was analyzed by FlowJo_V10.

Apoptosis analysis—1×10^6 of 22Rv1 cells were suspended by trypsinization and washed twice with cold PBS. The cell pellet was resuspended in 1 ml 1X Binding Buffer (BD Pharmingen™ BDB559763). 100 μl of cell suspension was transferred to a 5 ml culture tube and added with 5 μl PE Annexin V and 5 μl 7-AAD (BD Pharmingen™ BDB559763). The cell suspension was gently vortexed and incubated for 15 min at RT in dark. 400 μl of 1X Binding Buffer was added to each tube and analyzed by flow cytometry. Unstained cells, single PE Annexin V and single 7-AAD stained cells were used for control. The data was analyzed by FlowJo_V10.

Protein co-immunoprecipitation (co-IP)—Immunoprecipitations were performed as described previously [74]. Briefly, cells were lysed with lysis buffer (50 mM Tris-HCl pH 7.5, 150 mM NaCl, 0.1% Nonidet P-40, and freshly added protease inhibitor cocktails) and centrifuged to obtain supernatant. Protein A/G beads and indicated antibody were used to incubate with the supernatant at 4 °C overnight. Beads were washed 3 times with lysis buffer, re-suspended in SDS loading buffer prior to western blot analysis.

Western blot—Whole cell lysates or IP samples were subjected to SDS-PAGE. The proteins were transferred onto nitrocellulose membranes (GE Healthcare sciences). The transferred membranes were blocked using TBST with 5% w/v nonfat milk and incubated with indicated primary antibodies at 4 °C overnight. The antibodies used in this study were listed in the Key Resources Table. In the second day, the membranes were washed 3 times with TBST and followed by incubation with secondary antibodies at room temperature.

After washing in TBST for three times, the membranes were visualized using Enhanced Chemiluminescence (ECL) system (Thermo Fisher Scientific).

Cell proliferation assay—Cells were seeded in 96-well plates in a concentration of 2,000 cells per well. The CellTiter 96 Aqueous One solution Cell Proliferation Assay (MTS) (Promega) was used to measure cell viability at indicated time points as described previously [71]. The MTS was diluted at a ratio of 1:10 in PBS and added into the wells and incubated for 1 h at 37 °C in a cell incubator. Microplate reader was used to measure absorbance of 490 nm in each well.

Colony formation assay—The procedure was carried out as previously described [74]. Briefly, cells were seeded in 6-well plates in a concentration of 5,000 cells per well. Approximately 12 days later, the colonies were fixed with 4% paraformaldehyde for 15 min and stained with crystal violet (0.5% w/v) for 1 h. The colonies were gently washed with running tap water and counted for quantification.

Xenografts generation and drug treatment—The animal studies were approved by the Institutional Animal Care and Use Committee (IACUC) at the Mayo Clinic. Six-week-old SCID male mice were housed in standard condition with a 12-h light /12-h dark cycle and randomly divided into different groups as indicated. 5×10^6 of mock KO or *FTO-IT1* KO C4–2R cells were mixed with Matrigel (50 μl of PBS plus 50 μl of Matrigel (BD Biosciences)) and injected subcutaneously into mice. For 22Rv1 xenografts, 5×10^6 of cells were mixed with Matrigel (50 μl of PBS plus 50 μl of Matrigel (BD Biosciences)) and injected subcutaneously into mice. When xenografts reached a size of approximately 100 mm^3, indicated vehicle (PBS with 0.3 mg/ml PEI) and drugs (*FTO-IT1*-specific ASOs 3 mg/kg in PBS with 0.3 mg/ml PEI) were administered by tail vein injection 4 days a week. Tumor growth was measured in a blinded fashion by a caliper. The volume of the tumors was calculated using the formula $(L \times W2)/2$, where L stands for the length of the tumor and W stands for the width. Tumor volumes were compared, and *P* values were determined by unpaired two-tailed Student's *t*-test. After 3-week injection, the tumors were dissected and photographed.

TCGA gene expression and survival analysis—IlluminaHiSeq (n=550) TCGA Hub level-3 data was downloaded from TCGA data coordination center. This dataset shows the gene-level transcription estimates, as in log2(x+1) transformed RSEM normalized count. Genes are mapped onto the human genome coordinates using UCSC Xena HUGO probeMap (see ID/Gene mapping link below for details). The TCGA reference method description is from the University of North Carolina Center for Genomic Characterization: DCC description. In order to make it easier to see differential expression between samples, we set the default view to center each gene or exon independently minus each gene with mean zero or exons. For survival analysis, the cohort was split into high-expression and low-expression group using a function of the X-tile software[75] as a method for selection of optimal cutpoint. The *P* values were calculated by logrank test.

WCDT dataset survival analysis—Gene expression and clinical information for the PCa West Coast Dream Team (WCDT) dataset were downloaded from previous

publication [76]. For survival analysis, samples were median dichotomized into two groups according to *FTO-IT1* expression. Logrank test from the R package Survival (v3.2.11) was used to calculate *P* value and the result was visualized using the R package BoutrosLab.plotting.general (v5.9.8) [77].

Quantification and statistical analysis—All data are shown as means ± SD unless otherwise specified. The data was processed in Microsoft Excel version 2013. Difference between two groups were analyzed using unpaired two-tailed Student's *t*-tests unless otherwise specified. A *P* value < 0.05 was considered statistically significant.

Supplementary Material

Refer to Web version on PubMed Central for supplementary material.

Acknowledgements

We thank Drs. Yu Zhao, Sisi Chen and Daqiang Li for their assistance in this project. This work was supported in part by funding from the Mayo Clinic Foundation (to H.H.), Howard Hughes Medical Institute (to C.H.) and NIH (R01CA130908, R01CA203849 and R01 CA271486 to H.H. and R01ES030546 to C.H.). C.H. is a Howard Hughes Medical Institute Investigator.

C.H. is a scientific founder and a scientific advisory board member of Accent Therapeutics, Inc.; Aferna Bio, Inc.; and AccuraDX, Inc.

References

1. Shi H, Wei J, and He C. (2019). Where, When, and How: Context-Dependent Functions of RNA Methylation Writers, Readers, and Erasers. Mol Cell 74, 640–650. 10.1016/j.molcel.2019.04.025. [PubMed: 31100245]
2. Frye M, Harada BT, Behm M, and He C. (2018). RNA modifications modulate gene expression during development. Science 361, 1346–1349. 10.1126/science.aau1646. [PubMed: 30262497]
3. Liu J, Yue Y, Han D, Wang X, Fu Y, Zhang L, Jia G, Yu M, Lu Z, Deng X, et al. (2014). A METTL3-METTL14 complex mediates mammalian nuclear RNA N6-adenosine methylation. Nat Chem Biol 10, 93–95. 10.1038/nchembio.1432. [PubMed: 24316715]
4. Ping XL, Sun BF, Wang L, Xiao W, Yang X, Wang WJ, Adhikari S, Shi Y, Lv Y, Chen YS, et al. (2014). Mammalian WTAP is a regulatory subunit of the RNA N6-methyladenosine methyltransferase. Cell Res 24, 177–189. 10.1038/cr.2014.3. [PubMed: 24407421]
5. Patil DP, Chen CK, Pickering BF, Chow A, Jackson C, Guttman M, and Jaffrey SR (2016). m(6)A RNA methylation promotes XIST-mediated transcriptional repression. Nature 537, 369–373. 10.1038/nature19342. [PubMed: 27602518]
6. Wei J, Liu F, Lu Z, Fei Q, Ai Y, He PC, Shi H, Cui X, Su R, Klungland A, et al. . (2018). Differential m(6)A, m(6)Am, and m(1)A Demethylation Mediated by FTO in the Cell Nucleus and Cytoplasm. Mol Cell 71, 973–985 e975. 10.1016/j.molcel.2018.08.011. [PubMed: 30197295]
7. Jia G, Fu Y, Zhao X, Dai Q, Zheng G, Yang Y, Yi C, Lindahl T, Pan T, Yang YG, and He C. (2011). N6-methyladenosine in nuclear RNA is a major substrate of the obesity-associated FTO. Nat Chem Biol 7, 885–887. 10.1038/nchembio.687. [PubMed: 22002720]
8. Zheng G, Dahl JA, Niu Y, Fedorcsak P, Huang CM, Li CJ, Vagbo CB, Shi Y, Wang WL, Song SH, et al. (2013). ALKBH5 is a mammalian RNA demethylase that impacts RNA metabolism and mouse fertility. Mol Cell 49, 18–29. 10.1016/j.molcel.2012.10.015. [PubMed: 23177736]
9. Wei J, Yu X, Yang L, Liu X, Gao B, Huang B, Dou X, Liu J, Zou Z, Cui XL, et al. (2022). FTO mediates LINE1 m(6)A demethylation and chromatin regulation in mESCs and mouse development. Science 376, 968–973. 10.1126/science.abe9582. [PubMed: 35511947]

10. Sobreira DR, Joslin AC, Zhang Q, Williamson I, Hansen GT, Farris KM, Sakabe NJ, Sinnott-Armstrong N, Bozek G, Jensen-Cody SO, et al. (2021). Extensive pleiotropism and allelic heterogeneity mediate metabolic effects of IRX3 and IRX5. Science 372, 1085–1091. 10.1126/science.abf1008. [PubMed: 34083488]
11. Smemo S, Tena JJ, Kim KH, Gamazon ER, Sakabe NJ, Gomez-Marin C, Aneas I, Credidio FL, Sobreira DR, Wasserman NF, et al. (2014). Obesity-associated variants within FTO form long-range functional connections with IRX3. Nature 507, 371–375. 10.1038/nature13138. [PubMed: 24646999]
12. Dina C, Meyre D, Gallina S, Durand E, Korner A, Jacobson P, Carlsson LM, Kiess W, Vatin V, Lecoeur C, et al. (2007). Variation in FTO contributes to childhood obesity and severe adult obesity. Nat Genet 39, 724–726. 10.1038/ng2048. [PubMed: 17496892]
13. Gulati P, Cheung MK, Antrobus R, Church CD, Harding HP, Tung YC, Rimmington D, Ma M, Ron D, Lehner PJ, et al. (2013). Role for the obesity-related FTO gene in the cellular sensing of amino acids. Proc Natl Acad Sci U S A 110, 2557–2562. 10.1073/pnas.1222796110. [PubMed: 23359686]
14. Frayling TM, Timpson NJ, Weedon MN, Zeggini E, Freathy RM, Lindgren CM, Perry JR, Elliott KS, Lango H, Rayner NW, et al. (2007). A common variant in the FTO gene is associated with body mass index and predisposes to childhood and adult obesity. Science 316, 889–894. 10.1126/science.1141634. [PubMed: 17434869]
15. Scuteri A, Sanna S, Chen WM, Uda M, Albai G, Strait J, Najjar S, Nagaraja R, Orru M, Usala G, et al. (2007). Genome-wide association scan shows genetic variants in the FTO gene are associated with obesity-related traits. PLoS Genet 3, e115. 10.1371/journal.pgen.0030115. [PubMed: 17658951]
16. Church C, Moir L, McMurray F, Girard C, Banks GT, Teboul L, Wells S, Bruning JC, Nolan PM, Ashcroft FM, and Cox RD (2010). Overexpression of Fto leads to increased food intake and results in obesity. Nat Genet 42, 1086–1092. 10.1038/ng.713. [PubMed: 21076408]
17. el-Deiry WS, Tokino T, Velculescu VE, Levy DB, Parsons R, Trent JM, Lin D, Mercer WE, Kinzler KW, and Vogelstein B. (1993). WAF1, a potential mediator of p53 tumor suppression. Cell 75, 817–825. 10.1016/0092-8674(93)90500-p. [PubMed: 8242752]
18. Yu J, Zhang L, Hwang PM, Kinzler KW, and Vogelstein B. (2001). PUMA induces the rapid apoptosis of colorectal cancer cells. Mol Cell 7, 673–682. 10.1016/s1097-2765(01)00213-1. [PubMed: 11463391]
19. Nakano K, and Vousden KH. (2001). PUMA, a novel proapoptotic gene, is induced by p53. Mol Cell 7, 683–694. 10.1016/s1097-2765(01)00214-3. [PubMed: 11463392]
20. Okamura S, Arakawa H, Tanaka T, Nakanishi H, Ng CC, Taya Y, Monden M, and Nakamura Y. (2001). p53DINP1, a p53-inducible gene, regulates p53-dependent apoptosis. Mol Cell 8, 85–94. 10.1016/s1097-2765(01)00284-2. [PubMed: 11511362]
21. Owen-Schaub LB, Zhang W, Cusack JC, Angelo LS, Santee SM, Fujiwara T, Roth JA, Deisseroth AB, Zhang WW, Kruzel E, and et al. (1995). Wild-type human p53 and a temperature-sensitive mutant induce Fas/APO-1 expression. Mol Cell Biol 15, 3032–3040. 10.1128/MCB.15.6.3032. [PubMed: 7539102]
22. Budanov AV, and Karin M. (2008). p53 target genes sestrin1 and sestrin2 connect genotoxic stress and mTOR signaling. Cell 134, 451–460. 10.1016/j.cell.2008.06.028. [PubMed: 18692468]
23. Kon N, Ou Y, Wang SJ, Li H, Rustgi AK, and Gu W. (2021). mTOR inhibition acts as an unexpected checkpoint in p53-mediated tumor suppression. Genes Dev 35, 59–64. 10.1101/gad.340919.120. [PubMed: 33303641]
24. Lane DP (2019). How to lose tumor suppression. Science 365, 539–540. 10.1126/science.aay4319. [PubMed: 31395768]
25. Muller PA, and Vousden KH (2014). Mutant p53 in cancer: new functions and therapeutic opportunities. Cancer Cell 25, 304–317. 10.1016/j.ccr.2014.01.021. [PubMed: 24651012]
26. Kastenhuber ER, and Lowe SW (2017). Putting p53 in Context. Cell 170, 1062–1078. 10.1016/j.cell.2017.08.028. [PubMed: 28886379]

27. Robinson D, Van Allen EM, Wu YM, Schultz N, Lonigro RJ, Mosquera JM, Montgomery B, Taplin ME, Pritchard CC, Attard G, et al. (2015). Integrative clinical genomics of advanced prostate cancer. Cell 161, 1215–1228. 10.1016/j.cell.2015.05.001. [PubMed: 26000489]

28. Huang J, Sengupta R, Espejo AB, Lee MG, Dorsey JA, Richter M, Opravil S, Shiekhattar R, Bedford MT, Jenuwein T, and Berger SL (2007). p53 is regulated by the lysine demethylase LSD1. Nature 449, 105–108. 10.1038/nature06092. [PubMed: 17805299]

29. Wang D, Kon N, Lasso G, Jiang L, Leng W, Zhu WG, Qin J, Honig B, and Gu W. (2016). Acetylation-regulated interaction between p53 and SET reveals a widespread regulatory mode. Nature 538, 118–122. 10.1038/nature19759. [PubMed: 27626385]

30. Grossmann ME, Huang H, and Tindall DJ (2001). Androgen receptor signaling in androgen-refractory prostate cancer. J Natl Cancer Inst 93, 1687–1697. 10.1093/jnci/93.22.1687. [PubMed: 11717329]

31. Watson PA, Arora VK, and Sawyers CL (2015). Emerging mechanisms of resistance to androgen receptor inhibitors in prostate cancer. Nat Rev Cancer 15, 701–711. 10.1038/nrc4016. [PubMed: 26563462]

32. Tran C, Ouk S, Clegg NJ, Chen Y, Watson PA, Arora V, Wongvipat J, Smith-Jones PM, Yoo D, Kwon A, et al. (2009). Development of a second-generation antiandrogen for treatment of advanced prostate cancer. Science 324, 787–790. 10.1126/science.1168175. [PubMed: 19359544]

33. Scher HI, Fizazi K, Saad F, Taplin ME, Sternberg CN, Miller K, de Wit R, Mulders P, Chi KN, Shore ND, et al. (2012). Increased survival with enzalutamide in prostate cancer after chemotherapy. N Engl J Med 367, 1187–1197. 10.1056/NEJMoa1207506. [PubMed: 22894553]

34. Tannock IF, de Wit R, Berry WR, Horti J, Pluzanska A, Chi KN, Oudard S, Theodore C, James ND, Turesson I, et al. . (2004). Docetaxel plus prednisone or mitoxantrone plus prednisone for advanced prostate cancer. N Engl J Med 351, 1502–1512. 10.1056/NEJMoa040720. [PubMed: 15470213]

35. Petrylak DP, Tangen CM, Hussain MH, Lara PN Jr., Jones JA, Taplin ME, Burch PA, Berry D, Moinpour C, Kohli M, et al. (2004). Docetaxel and estramustine compared with mitoxantrone and prednisone for advanced refractory prostate cancer. N Engl J Med 351, 1513–1520. 10.1056/NEJMoa041318. [PubMed: 15470214]

36. Gan L, Chen S, Wang Y, Watahiki A, Bohrer L, Sun Z, Wang Y, and Huang H. (2009). Inhibition of the androgen receptor as a novel mechanism of taxol chemotherapy in prostate cancer. Cancer Res 69, 8386–8394. 10.1158/0008-5472.CAN-09-1504. [PubMed: 19826044]

37. Kuroda K, Liu H, Kim S, Guo M, Navarro V, and Bander NH (2009). Docetaxel down-regulates the expression of androgen receptor and prostate-specific antigen but not prostate-specific membrane antigen in prostate cancer cell lines: implications for PSA surrogacy. Prostate 69, 1579–1585. 10.1002/pros.21004. [PubMed: 19575420]

38. Zhu ML, Horbinski CM, Garzotto M, Qian DZ, Beer TM, and Kyprianou N. (2010). Tubulin-targeting chemotherapy impairs androgen receptor activity in prostate cancer. Cancer Res 70, 7992–8002. 10.1158/0008-5472.CAN-10-0585. [PubMed: 20807808]

39. Darshan MS, Loftus MS, Thadani-Mulero M, Levy BP, Escuin D, Zhou XK, Gjyrezi A, Chanel-Vos C, Shen R, Tagawa ST, et al. (2011). Taxane-induced blockade to nuclear accumulation of the androgen receptor predicts clinical responses in metastatic prostate cancer. Cancer Res 71, 6019–6029. 10.1158/0008-5472.CAN-11-1417. [PubMed: 21799031]

40. Zhao J, Zhao Y, Wang L, Zhang J, Karnes RJ, Kohli M, Wang G, and Huang H. (2016). Alterations of androgen receptor-regulated enhancer RNAs (eRNAs) contribute to enzalutamide resistance in castration-resistant prostate cancer. Oncotarget 7, 38551–38565. 10.18632/oncotarget.9535. [PubMed: 27221037]

41. Zhao Y, Wang L, Ren S, Wang L, Blackburn PR, McNulty MS, Gao X, Qiao M, Vessella RL, Kohli M, et al. (2016). Activation of P-TEFb by Androgen Receptor-Regulated Enhancer RNAs in Castration-Resistant Prostate Cancer. Cell Rep 15, 599–610. 10.1016/j.celrep.2016.03.038. [PubMed: 27068475]

42. Wen S, Niu Y, and Huang H. (2020). Posttranslational regulation of androgen dependent and independent androgen receptor activities in prostate cancer. Asian J Urol 7, 203–218. 10.1016/j.ajur.2019.11.001. [PubMed: 33024699]

43. Blatt EB, and Raj GV (2019). Molecular mechanisms of enzalutamide resistance in prostate cancer. Cancer Drug Resist 2, 189–197. 10.20517/cdr.2019.25. [PubMed: 35582713]
44. Li Y, Chan SC, Brand LJ, Hwang TH, Silverstein KA, and Dehm SM (2013). Androgen receptor splice variants mediate enzalutamide resistance in castration-resistant prostate cancer cell lines. Cancer Res 73, 483–489. 10.1158/0008-5472.CAN-12-3630. [PubMed: 23117885]
45. Neklesa T, Snyder LB, Willard RR, Vitale N, Raina K, Pizzano J, Gordon D, Bookbinder M, Macaluso J, Dong H, et al. (2018). Abstract 5236: ARV-110: An androgen receptor PROTAC degrader for prostate cancer. cancer research 78 (Supplement).
46. Mauer J, Luo X, Blanjoie A, Jiao X, Grozhik AV, Patil DP, Linder B, Pickering BF, Vasseur JJ, Chen Q, et al. (2017). Reversible methylation of m(6)Am in the 5' cap controls mRNA stability. Nature 541, 371–375. 10.1038/nature21022. [PubMed: 28002401]
47. Dominissini D, Moshitch-Moshkovitz S, Schwartz S, Salmon-Divon M, Ungar L, Osenberg S, Cesarkas K, Jacob-Hirsch J, Amariglio N, Kupiec M, et al. . (2012). Topology of the human and mouse m6A RNA methylomes revealed by m6A-seq. Nature 485, 201–206. 10.1038/nature11112. [PubMed: 22575960]
48. Meyer KD, Saletore Y, Zumbo P, Elemento O, Mason CE, and Jaffrey SR (2012). Comprehensive analysis of mRNA methylation reveals enrichment in 3' UTRs and near stop codons. Cell 149, 1635–1646. 10.1016/j.cell.2012.05.003. [PubMed: 22608085]
49. Budanov AV, Shoshani T, Faerman A, Zelin E, Kamer I, Kalinski H, Gorodin S, Fishman A, Chajut A, Einat P, et al. (2002). Identification of a novel stress-responsive gene Hi95 involved in regulation of cell viability. Oncogene 21, 6017–6031. 10.1038/sj.onc.1205877. [PubMed: 12203114]
50. Muller M, Wilder S, Bannasch D, Israeli D, Lehlbach K, Li-Weber M, Friedman SL, Galle PR, Stremmel W, Oren M, and Krammer PH (1998). p53 activates the CD95 (APO-1/Fas) gene in response to DNA damage by anticancer drugs. J Exp Med 188, 2033–2045. 10.1084/jem.188.11.2033. [PubMed: 9841917]
51. Tai H, Wang X, Zhou J, Han X, Fang T, Gong H, Huang N, Chen H, Qin J, Yang M, et al. (2017). Protein kinase Cbeta activates fat mass and obesity-associated protein by influencing its ubiquitin/proteasome degradation. FASEB J 31, 4396–4406. 10.1096/fj.201601159RR. [PubMed: 28626026]
52. Appel L-M, Franke V, Benedum J, Grishkovskaya I, Strobl X, Polyansky A, Ammann G, Platzer S, Neudolt A, Wunder A, et al. (2023). The SPOC domain is a phosphoserine binding module that bridges transcription machinery with co- and posttranscriptional regulators. Nature Communications 14, 166. 10.1038/s41467-023-35853-1.
53. Huang H, Weng H, Sun W, Qin X, Shi H, Wu H, Zhao BS, Mesquita A, Liu C, Yuan CL, et al. (2018). Recognition of RNA N(6)-methyladenosine by IGF2BP proteins enhances mRNA stability and translation. Nat Cell Biol 20, 285–295. 10.1038/s41556-018-0045-z. [PubMed: 29476152]
54. Wang X, Lu Z, Gomez A, Hon GC, Yue Y, Han D, Fu Y, Parisien M, Dai Q, Jia G, et al. (2014). N6-methyladenosine-dependent regulation of messenger RNA stability. Nature 505, 117–120. 10.1038/nature12730. [PubMed: 24284625]
55. Wang X, Zhao BS, Roundtree IA, Lu Z, Han D, Ma H, Weng X, Chen K, Shi H, and He C. (2015). N(6)-methyladenosine Modulates Messenger RNA Translation Efficiency. Cell 161, 1388–1399. 10.1016/j.cell.2015.05.014. [PubMed: 26046440]
56. Hsu PJ, Zhu Y, Ma H, Guo Y, Shi X, Liu Y, Qi M, Lu Z, Shi H, Wang J, et al. (2017). Ythdc2 is an N(6)-methyladenosine binding protein that regulates mammalian spermatogenesis. Cell Res 27, 1115–1127. 10.1038/cr.2017.99. [PubMed: 28809393]
57. Roundtree IA, Luo GZ, Zhang Z, Wang X, Zhou T, Cui Y, Sha J, Huang X, Guerrero L, Xie P, et al. (2017). YTHDC1 mediates nuclear export of N(6)-methyladenosine methylated mRNAs. Elife 6. 10.7554/eLife.31311.
58. Shi H, Wang X, Lu Z, Zhao BS, Ma H, Hsu PJ, Liu C, and He C. (2017). YTHDF3 facilitates translation and decay of N(6)-methyladenosine-modified RNA. Cell Res 27, 315–328. 10.1038/cr.2017.15. [PubMed: 28106072]

59. Xiao W, Adhikari S, Dahal U, Chen YS, Hao YJ, Sun BF, Sun HY, Li A, Ping XL, Lai WY, et al. (2016). Nuclear m(6)A Reader YTHDC1 Regulates mRNA Splicing. Mol Cell 61, 507–519. 10.1016/j.molcel.2016.01.012. [PubMed: 26876937]
60. Sigal A, and Rotter V. (2000). Oncogenic mutations of the p53 tumor suppressor: the demons of the guardian of the genome. Cancer Res 60, 6788–6793. [PubMed: 11156366]
61. Barnoud T, Indeglia A, and Murphy ME (2021). Shifting the paradigms for tumor suppression: lessons from the p53 field. Oncogene 40, 4281–4290. 10.1038/s41388-021-01852-z. [PubMed: 34103683]
62. Boutelle AM, and Attardi LD (2021). p53 and Tumor Suppression: It Takes a Network. Trends Cell Biol 31, 298–310. 10.1016/j.tcb.2020.12.011. [PubMed: 33518400]
63. Raj N, Wang M, Seoane JA, Zhao RL, Kaiser AM, Moonie NA, Demeter J, Boutelle AM, Kerr CH, Mulligan AS, et al. (2022). The Mettl3 epitranscriptomic writer amplifies p53 stress responses. Mol Cell 82, 2370–2384 e2310. 10.1016/j.molcel.2022.04.010. [PubMed: 35512709]
64. He PC, Wei J, Dou X, Harada BT, Zhang Z, Ge R, Liu C, Zhang LS, Yu X, Wang S, et al. (2023). Exon architecture controls mRNA m(6)A suppression and gene expression. Science 379, 677–682. 10.1126/science.abj9090. [PubMed: 36705538]
65. Raj N, Wang M, Seoane JA, Zhao RL, Kaiser AM, Moonie NA, Demeter J, Boutelle AM, Kerr CH, Mulligan AS, et al. (2022). The Mettl3 epitranscriptomic writer amplifies p53 stress responses. Mol Cell. 10.1016/j.molcel.2022.04.010.
66. Wei J, and He C. (2021). Chromatin and transcriptional regulation by reversible RNA methylation. Curr Opin Cell Biol 70, 109–115. 10.1016/j.ceb.2020.11.005. [PubMed: 33706173]
67. Shalem O, Sanjana NE, Hartenian E, Shi X, Scott DA, Mikkelson T, Heckl D, Ebert BL, Root DE, Doench JG, and Zhang F. (2014). Genome-scale CRISPR-Cas9 knockout screening in human cells. Science 343, 84–87. 10.1126/science.1247005. [PubMed: 24336571]
68. Tripathi V, Fei J, Ha T, and Prasanth KV (2015). RNA fluorescence in situ hybridization in cultured mammalian cells. Methods Mol Biol 1206, 123–136. 10.1007/978-1-4939-1369-5_11. [PubMed: 25240892]
69. Bolger AM, Lohse M, and Usadel B. (2014). Trimmomatic: a flexible trimmer for Illumina sequence data. Bioinformatics 30, 2114–2120. 10.1093/bioinformatics/btu170. [PubMed: 24695404]
70. Drewe-Boss P, Wessels HH, and Ohler U. (2018). omniCLIP: probabilistic identification of protein-RNA interactions from CLIP-seq data. Genome Biol 19, 183. 10.1186/s13059-018-1521-2. [PubMed: 30384847]
71. Yang Y, Blee AM, Wang D, An J, Pan Y, Yan Y, Ma T, He Y, Dugdale J, Hou X, et al. (2017). Loss of FOXO1 Cooperates with TMPRSS2-ERG Overexpression to Promote Prostate Tumorigenesis and Cell Invasion. Cancer Res 77, 6524–6537. 10.1158/0008-5472.CAN-17-0686. [PubMed: 28986382]
72. Zhang P, Wang D, Zhao Y, Ren S, Gao K, Ye Z, Wang S, Pan CW, Zhu Y, Yan Y, et al. (2017). Intrinsic BET inhibitor resistance in SPOP-mutated prostate cancer is mediated by BET protein stabilization and AKT-mTORC1 activation. Nat Med 23, 1055–1062. 10.1038/nm.4379. [PubMed: 28805822]
73. Wang L, Dehm SM, Hillman DW, Sicotte H, Tan W, Gormley M, Bhargava V, Jimenez R, Xie F, Yin P, et al. (2018). A prospective genome-wide study of prostate cancer metastases reveals association of wnt pathway activation and increased cell cycle proliferation with primary resistance to abiraterone acetate-prednisone. Ann Oncol 29, 352–360. 10.1093/annonc/mdx689. [PubMed: 29069303]
74. Zhang J, Gao K, Xie H, Wang D, Zhang P, Wei T, Yan Y, Pan Y, Ye W, Chen H, et al. (2021). SPOP mutation induces DNA methylation via stabilizing GLP/G9a. Nat Commun 12, 5716. 10.1038/s41467-021-25951-3. [PubMed: 34588438]
75. Camp RL, Dolled-Filhart M, and Rimm DL. (2004). X-tile: a new bio-informatics tool for biomarker assessment and outcome-based cut-point optimization. Clin Cancer Res 10, 7252–7259. 10.1158/1078-0432.CCR-04-0713. [PubMed: 15534099]

76. Quigley DA, Dang HX, Zhao SG, Lloyd P, Aggarwal R, Alumkal JJ, Foye A, Kothari V, Perry MD, Bailey AM, et al. (2018). Genomic Hallmarks and Structural Variation in Metastatic Prostate Cancer. Cell 174, 758–769 e759. 10.1016/j.cell.2018.06.039. [PubMed: 30033370]

77. P'ng C, Green J, Chong LC, Waggott D, Prokopec SD, Shamsi M, Nguyen F, Mak DYF, Lam F, Albuquerque MA, et al. (2019). BPG: Seamless, automated and interactive visualization of scientific data. BMC Bioinformatics 20, 42. 10.1186/s12859-019-2610-2. [PubMed: 30665349]

Highlights

FTO-IT1 upregulation associates with poor prognosis of advanced prostate cancer

FTO-IT1 binds RBM15 and acts as an inhibitor of the m^6A 'writer' complex

FTO-IT1 inhibits p53 target gene mRNA m^6A level, phenocopying p53 inactivation

FTO-IT1 represents a viable therapeutic target of cancers

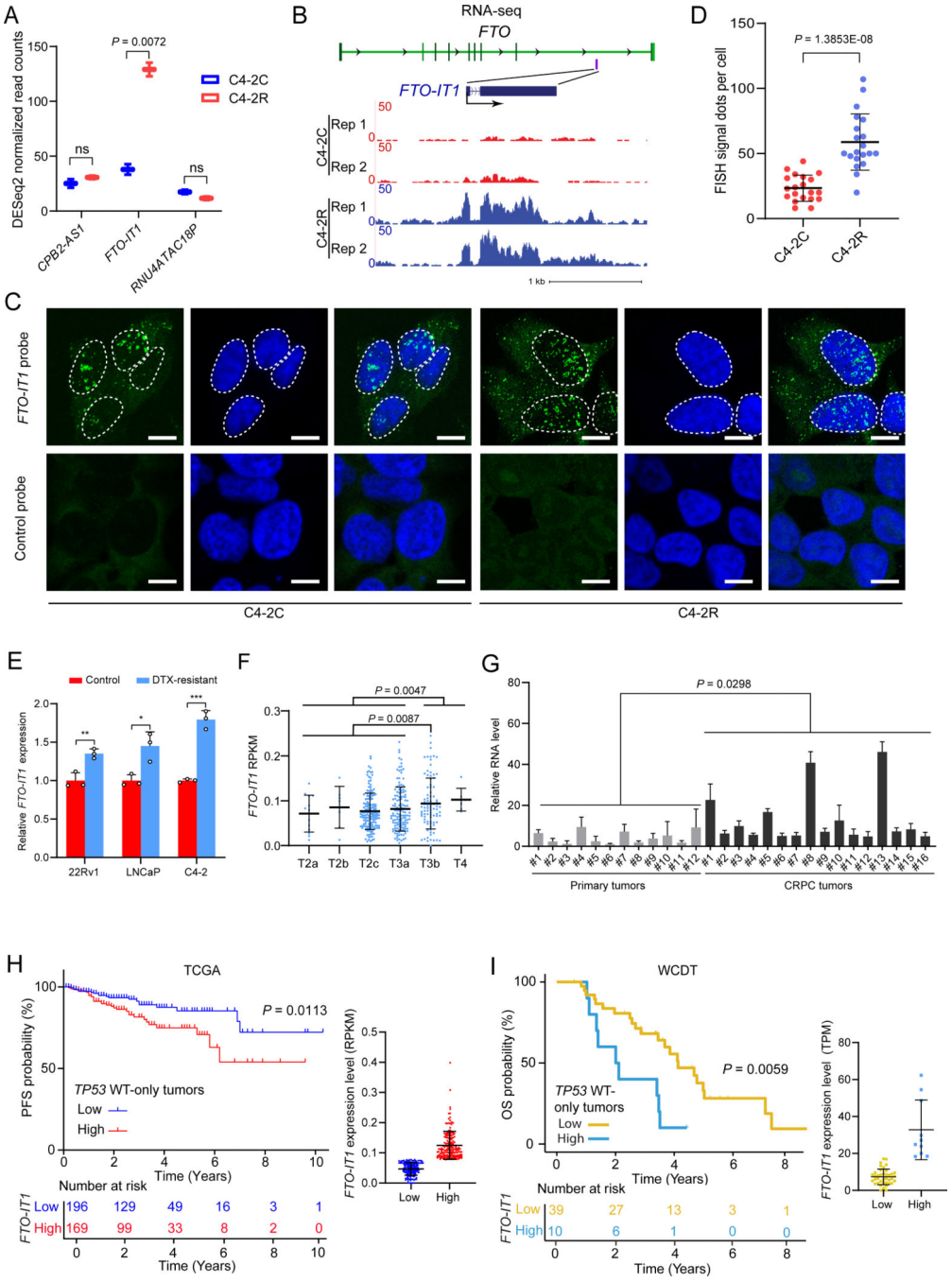

Figure 1. Increased expression of *FTO-IT1* associates with PCa progression and growth

(**A**) A boxplot of RNA-seq data showing upregulation of *FTO-IT1* ncRNA in C4–2R versus C4–2C cells.

(**B**) Diagram showing the location of *FTO-IT1* in the *FTO* gene locus (Above) and UCSC screenshot of RNA-seq profile showing the sequencing signal of *FTO-IT1* in C4–2R versus C4–2C cells (Bottom).

(**C**) RNA fluorescent in situ hybridization (FISH) of *FTO-IT1* using FAM-labeled *FTO-IT1* specific probes and antisense control probes in C4–2C and C4–2R cells. Scale bar, 10 μm.

(**D**) Quantification of *FTO-IT1* FISH signal in C4–2C and C4–2R cells.
(**E**) RT-qPCR of *FTO-IT1* in control and DTX-resistant 22Rv1, LNCaP and C4–2 cells.
(**F**) Comparison of *FTO-IT1* expression levels in different stages of prostate tumors in patients from the TCGA (Firehose Legacy) dataset.
(**G**) RT-qPCR analysis of *FTO-IT1* expression in primary PCa (n = 12) and CRPC (n = 16) patient samples.
(**H**) Probability of progression free survival (PFS) of *FTO-IT1*-high and *FTO-IT1*-low patients of the TCGA (Firehose Legacy) cohort with tumors expressing WT *TP53* (Left), and the expression data of *FTO-IT1* high and *FTO-IT1* low samples (Right). *P* values were calculated using logrank test.
(**I**) Probability of overall survival (OS) of *FTO-IT1*-high and *FTO-IT1*-low patients of the WCDT cohort with tumors expressing WT *TP53* (Left), and the expression data of *FTO-IT1* high and *FTO-IT1* low samples (Right). *P* values were calculated using logrank test.
A, D, E, F, G, Data shown as means ± SD. The *P* values were calculated using an unpaired two-tailed Student's *t*-test, $*P < 0.05$, $***P < 0.01$, $***P < 0.001$. Experiments in C, D, E, G were repeated twice.

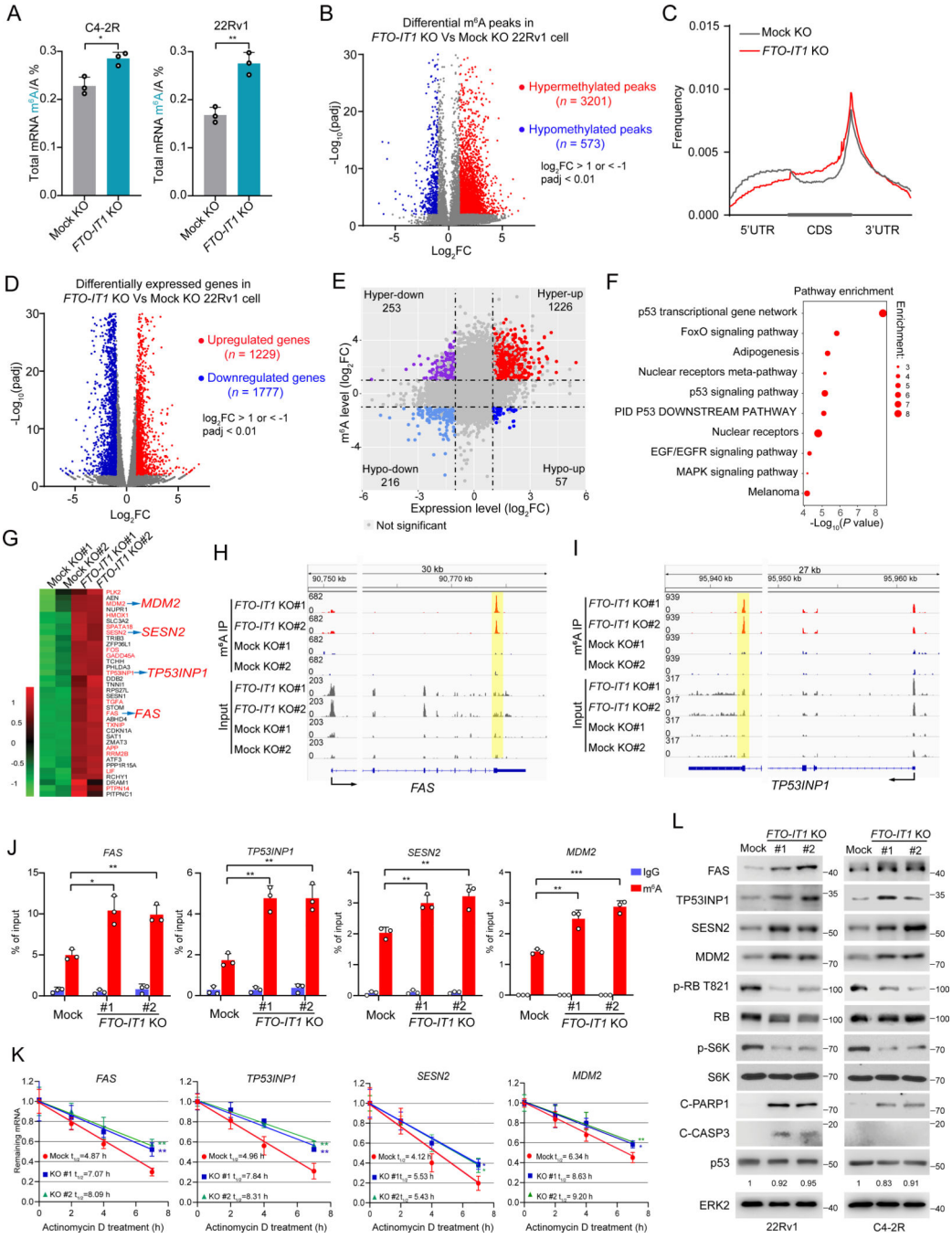

Figure 2. *FTO-IT1* downregulates p53 transcriptional target gene mRNA expression through m^{6}A modification

(**A**) Mass spectrometry analysis of global m^{6}A level on mRNAs from mock and *FTO-IT1* KO C4–2R and 22Rv1 cells.

(**B**) Volcano plot of the hyper- and hypomethylated peaks in *FTO-IT1* KO versus mock KO 22Rv1 cells.

(**C**) Overall m^{6}A frequencies along the indicated different regions of mRNAs in mock KO and *FTO-IT1* KO 22Rv1 cells.

(**D**) Volcano plot of the upregulated and downregulated genes in *FTO-IT1* KO versus mock KO 22Rv1 cells.
(**E**) Scatter plot showing the distribution of m^6A peaks with significant change in both m^6A level and expression level of corresponding genes in *FTO-IT1* KO versus mock KO 22Rv1 cells.
(**F**) Analysis of the enrichment of pathways from three databases (WikiPathways, KEGG Pathway, and Canonical Pathways) in the genes upregulated and hypermethylated in *FTO-IT1* KO compared to mock KO 22Rv1 cells.
(**G**) Heatmap showing the upregulated expression of p53 transcriptional target genes in *FTO-IT1* KO compared to mock KO 22Rv1 cells. The red labelled genes are hypermethylated upon *FTO-IT1* KO.
(**H, I**) IVG screenshot showing input RNA-seq and m^6A-seq signal profiles of *FAS* (**H**) and *TP53INP1* (**I**) gene loci in mock KO and *FTO-IT1* KO 22Rv1 cells.
(**J**) RIP-qPCR of the indicated genes from m^6A-immunoprecipitated mRNAs in mock KO and *FTO-IT1* KO 22Rv1 cells.
(**K**) Analysis of stability of the indicated gene mRNAs in 22Rv1 cells treated with actinomycin D for different periods of time.
(**L**) Western blots of whole cell lysates (WCL) from mock KO and *FTO-IT1* KO C4–2R and 22Rv1 cells. Short-exposure (S.E.) WB bands of p53 were quantified and normalized to ERK2 (loading control).
J, K, Data shown as means ± SD (n = 3 biological replicates). The *P* values were calculated using an unpaired two-tailed Student's *t*-test; $*P < 0.05$, $**P < 0.01$, $***P < 0.001$. Experiments in J-L were repeated twice.

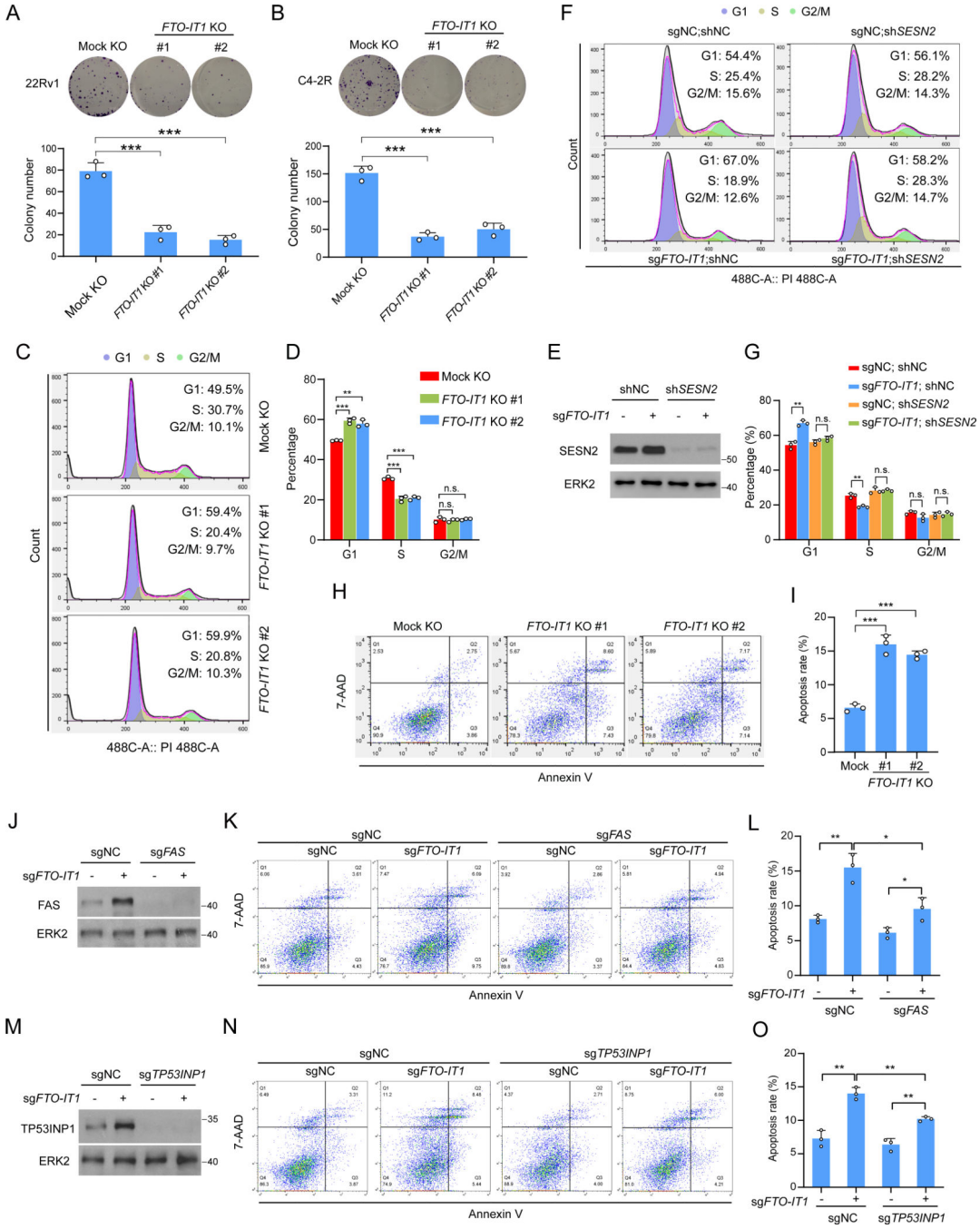

Figure 3. *FTO-IT1* promotes cell cycle progression and survival via p53 downstream pathways

(**A, B**) Colony formation and quantification of mock KO and *FTO-IT1* KO 22Rv1 (**A**) and C4–2R (**B**) cells.

(**C, D**) Cell cycle analysis of mock KO and *FTO-IT1* KO 22Rv1 cells using flow cytometry. Representative flow cytometry images (**C**) and quantification data (**D**) are presented.

(**E**) Western blot of WCL from mock KO and *FTO-IT1* KO 22Rv1 cells expressing control or *SESN2*-specific shRNA.

(**F, G**) Representative flow cytometry images (**F**) and quantification data (**G**) of mock KO and *FTO-IT1* KO 22Rv1 cells expressing control or *SESN2*-specific shRNA.
(**H, I**) Apoptosis analysis of mock KO and *FTO-IT1* KO 22Rv1 cells by flow cytometry. Representative flow cytometry images (**H**) and quantification data (**I**) are presented.
(**J-L**) Western blot (**J**) and apoptosis (**K, L**) analyses in mock KO and *FTO-IT1* KO 22Rv1 cells expressing control or *FAS*-specific sgRNA.
(**M-O**) Western blot (**M**) and apoptosis (**N, O**) analyses in mock KO and *FTO-IT1* KO 22Rv1 cells expressing control or *TP53INP1*-specific sgRNA.
A, B, D, G, I, L, O, Data shown as means ± SD (n = 3 biological replicates). The *P* values were calculated using an unpaired two-tailed Student's *t*-test; **P* < 0.05, ***P* < 0.01, ****P* < 0.001, n.s., not significant. Experiments in **A, B** were repeated twice.

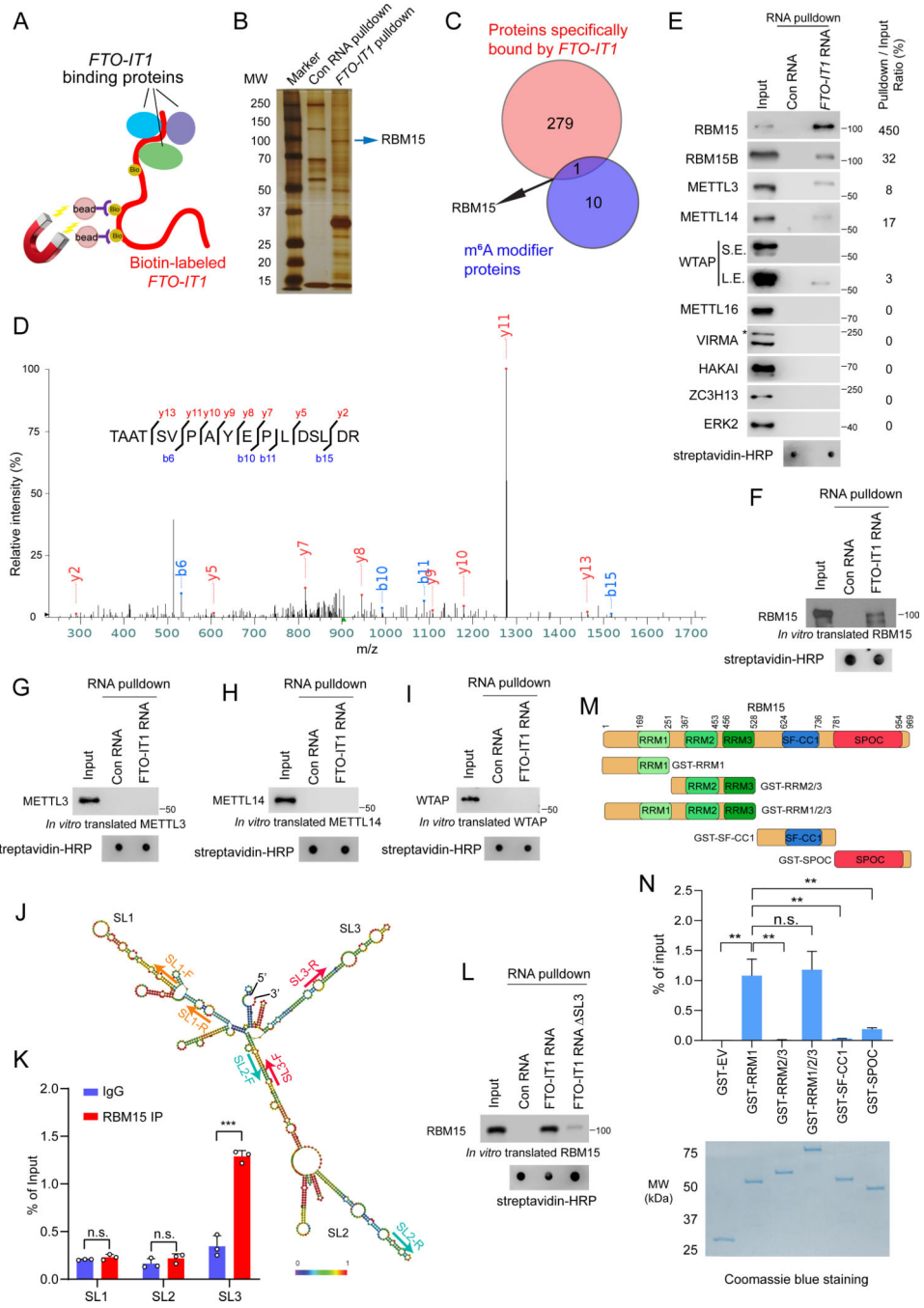

Figure 4. *FTO-IT1* interaction with RBM15 and the METTL3/14 MTase complex

(**A**) Diagram showing the working principle of protein-RNA pulled down assay using biotin-labeled *FTO-IT1* RNA as probe.

(**B**) Silver staining of proteins pulled down by control (con) RNA and *FTO-IT1.*

(**C**) Venn diagram showing the *FTO-IT1* interacting proteins and the major known m^{6}A modifier proteins (11 m^{6}A writers and erasers).

(**D**) Mass spectrum of the indicated unique peptide of RBM15.

(**E**) Western blot of indicated proteins in WCL and RNA pulldown samples. S.E. short exposure, L.E. long exposure, * non-specific band.

(**F-I**) Western blot of samples from RNA pulldown assays using *in vitro* translated RBM15, METTL3, METTL14 or WTAP.

(**J**) 2D structure of *FTO-IT1* predicted by RNAfold webserver (http://rna.tbi.univie.ac.at//cgi-bin/RNAWebSuite/RNAfold.cgi) and the primer pairs used to detect the indicated stem-loop regions.

(**K**) CLIP-qPCR analysis of indicated *FTO-IT1* regions using specific primers shown in (**J**) with the RBM15-immunoprecipitated RNAs from UV-crosslinked 22Rv1 cells transfected with *FTO-IT1* expression vector.

(**L**) Western blot of RBM15 protein pulled down by *FTO-IT1* full-length or SL3-deletion mutant (FTO-IT1ΔSL3) in RNA pulldown assays.

(**M, N**) GST-RBM15 recombinant protein constructs (**M**) and RT-qPCR analysis of samples from in vitro RNA binding assays using *in vitro* transcribed *FTO-IT1* RNA (**N**, top) and GST RBM15 recombinant proteins detected by Coomassie blue staining (**N**, bottom). **K, N**, Data shown as means ± SD (n = 3 biological replicates). Experiments in E-L were repeated twice.

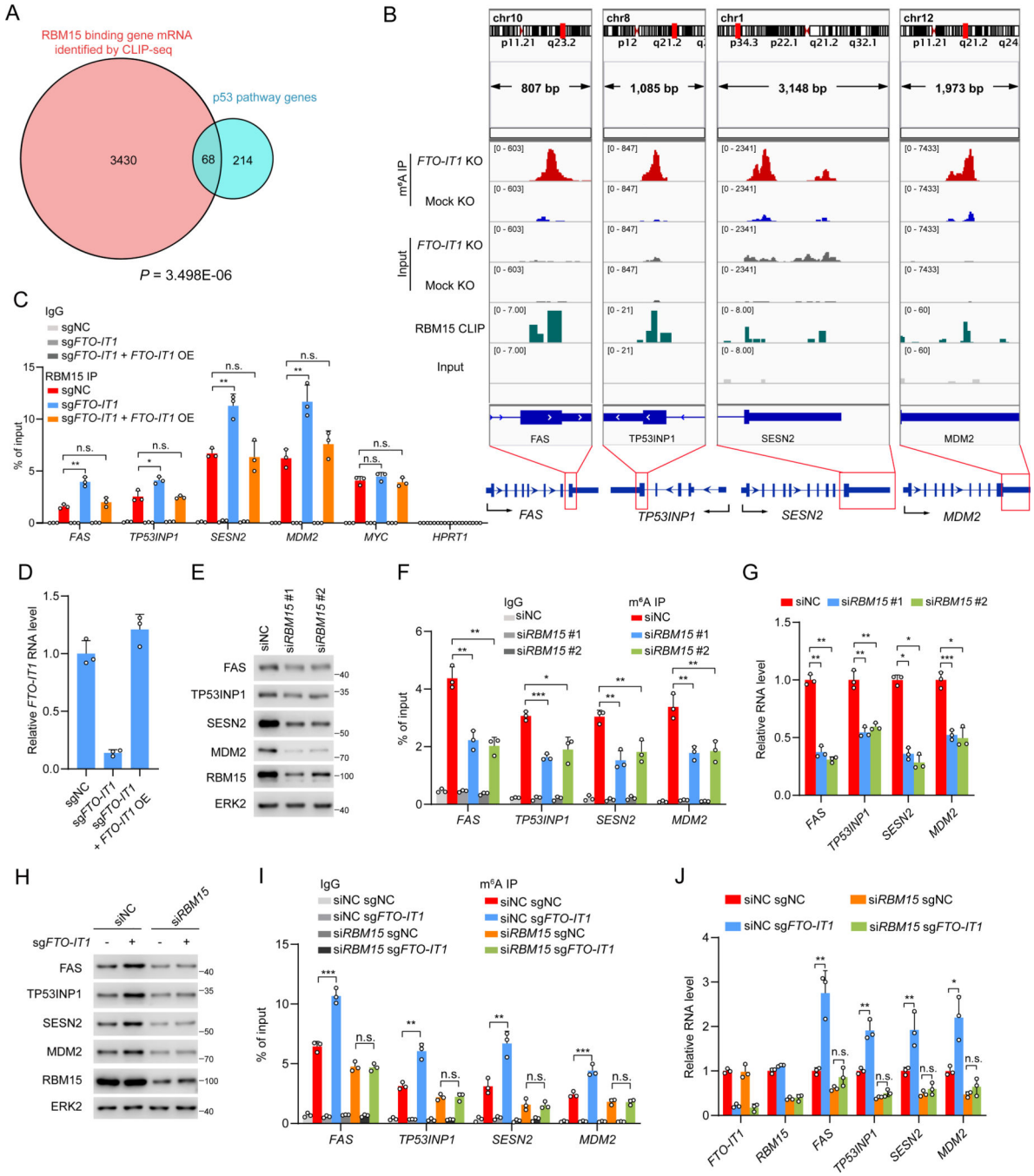

Figure 5. *FTO-IT1* regulates p53 transcriptional target gene expression via binding with RBM15

(**A**) Venn diagram showing the overlap between RBM15-interacting mRNAs identified by RBM15 CLIP-seq and typical p53 target gene mRNAs. *P* value was calculated by hypergeometric probability assuming 25,000 as the total gene number of humans.

(**B**) IVG screenshot of RBM15 CLIP-seq and m^{6}A RIP-seq in the indicated p53 target gene loci.

(**C**) CLIP-qPCR analysis of indicated mRNAs from RBM15-immunoprecipitated RNA from UV-crosslinked control, *FTO-IT1* KO, and *FTO-IT1*-rescued 22Rv1 cells.

(**D**) RT-qPCR analysis of *FTO-IT1* expression in control, *FTO-IT1* KO, and *FTO-IT1*-rescued 22Rv1 cells.
(**E**) Western blot of indicated proteins in WCL from 22Rv1 cells transfected with non-specific control (NC) or *RBM15*-specific siRNAs.
(**F**) RIP-qPCR of indicated genes in m^6A-immunoprecipitated mRNAs from 22Rv1 cells transfected with NC or *RBM15*-specific siRNAs.
(**G**) RT-qPCR of indicated genes from 22Rv1 cells transfected with NC or *RBM15*-specific siRNAs.
(**H**) Western blot of indicated proteins in WCL from control and *FTO-IT1* KO 22Rv1 cells transfected with NC or *RBM15*-specific siRNAs.
(**I**) RIP-qPCR of indicated genes from m^6A-immunoprecipitated mRNAs from control and *FTO-IT1* KO 22Rv1 cells transfected with NC or *RBM15*-specific siRNAs.
(**J**) RT-qPCR of indicated genes from control and *FTO-IT1* KO 22Rv1 cells transfected with NC or *RBM15*-specific siRNAs.
C, D, F, G, I, J, Data are shown as means ± SD (n = 3 biological replicates). The *P* values were calculated using an unpaired two-tailed Student's *t*-test; $*P < 0.05$, $**P < 0.01$, $***P < 0.001$, n.s., not significant. Experiments in **D**-**J** were repeated twice.

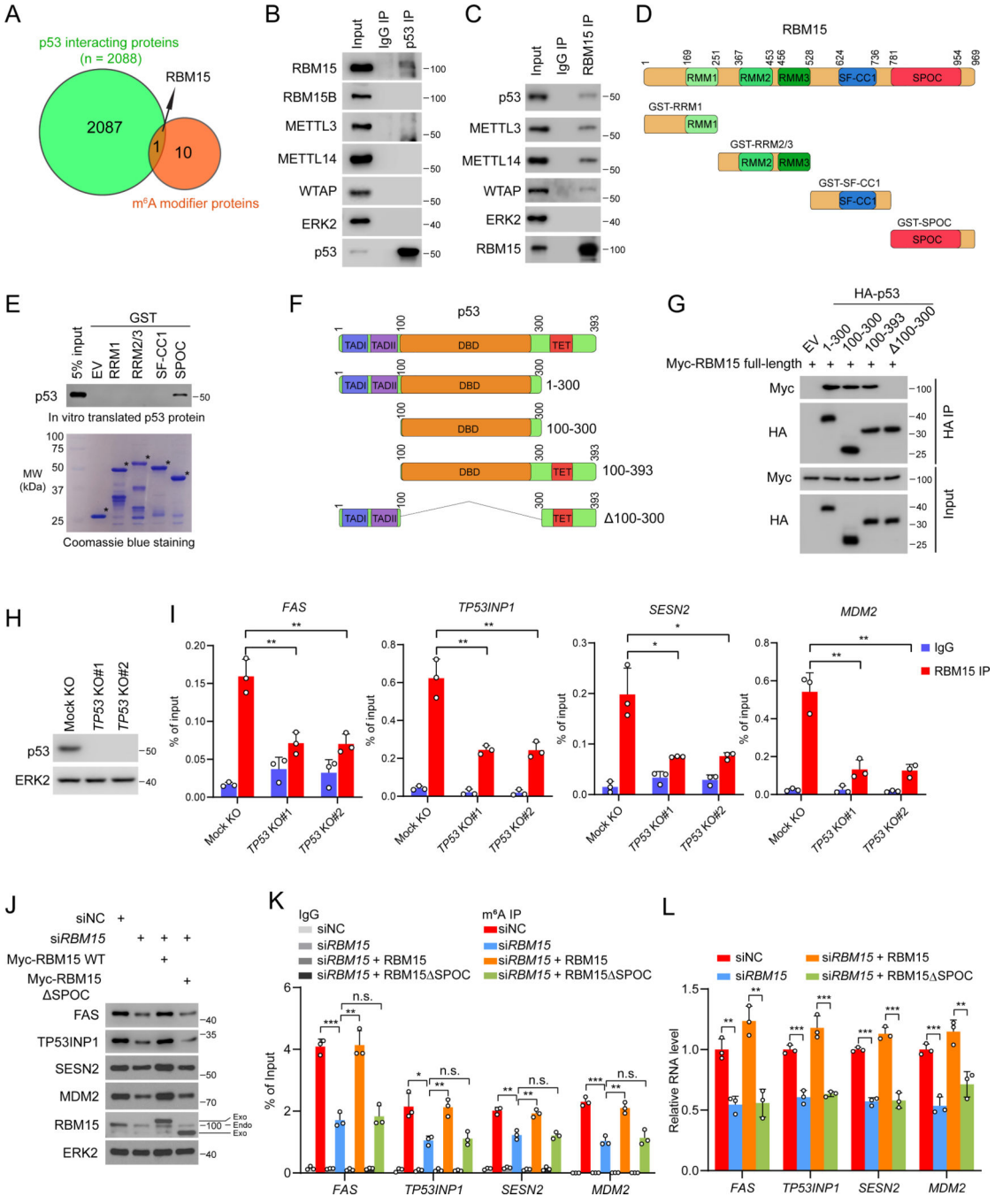

Figure 6. RBM15 binding of p53 is important for its regulation of p53 target mRNA m^{6}A level and expression

(**A**) Venn diagram showing the overlap between p53-interacting proteins (data from https://thebiogrid.org/) and the known m^{6}A writers and erasers.

(**B, C**) Western blot analysis of co-IP samples using IgG or indicated antibodies from cell lysate of 22Rv1 cells.

(**D, E**) GST pulldown using truncated GST-RBM15 recombinant proteins (**D**) and *in vitro* translated p53 protein followed by western blot analysis and Coomassie blue staining (**E**). Asterisks indicate the protein bands at the expected molecular weight.

(**F, G**) Co-IP assay using HA-tagged truncated p53 proteins (**F**) and Myc-tagged-RBM15 followed by western blot analysis (**G**).

(**H, I**) Western blot of proteins in indicated cells (**H**) and ChIP-qPCR analysis of RBM15 binding in the indicated gene promoters (except intron 1 of MDM2) in the RBM15-immunoprecipitated chromatin from formaldehyde crosslinked control and *TP53* KO 22Rv1 cells (**I**).

(**J-L**) Western blot (**J**), m^6A RIP-qPCR (**K**) and RT-qPCR (**L**) analyses in 22Rv1 cells transfected with indicate siRNAs and constructs.

I, K, L, Data shown as means ± SD (n = 3 biological replicates). The *P* values were calculated using an unpaired two-tailed Student's *t*-test; $*P < 0.05$, $**P < 0.01$, $***P < 0.001$, n.s., not significant. Experiments in **B, C, E, G, H, J** were repeated twice.

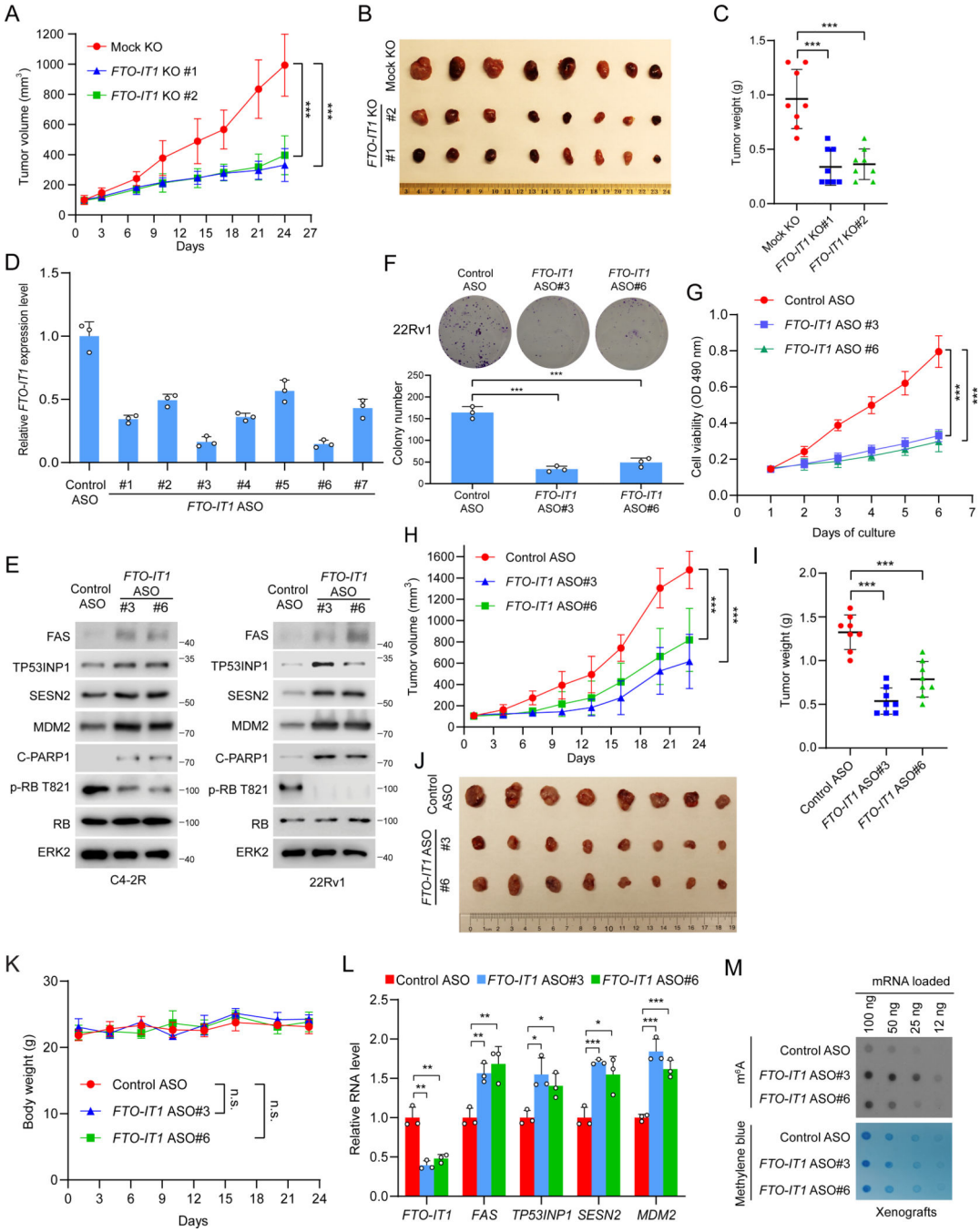

Figure 7. *FTO-IT1* regulation of PCa growth *in vitro* and in mice

(**A-C**) Measurement of growth (**A**), size and weight (day 24) (**B, C**) of tumors derived from mock and *FTO-IT1* KO C4–2R cells injected s.c. into SCID male mice.

(**D**) RT-qPCR analysis of *FTO-IT1* in 22Rv1 cells transfected with control or *FTO-IT1*-specific antisense oligos (ASOs).

(**E**) Western blot analysis of indicated proteins in C4–2R and 22Rv1 cells transfected with control or *FTO-IT1*-specific ASOs.

(**F, G**) Colony formation (**F**) and MTS (**G**) assays using 22Rv1 cells transfected as in (**E**).

(**H-K**) Measurement of growth (**H**), weight and size (day 24) (**I, J**) of tumors derived from 22Rv1 cells injected s.c. into SCID male mice and treated with control ASO or *FTO-IT1*-specific ASOs and mouse body weight (**K**).

(**L**) RT-qPCR analysis of *FTO-IT1* and indicated p53 target gene mRNAs in 22Rv1 xenografts harvested from the mice at 24 day after treated with control or *FTO-IT1*-specific ASOs as shown in (**H**).

(**M**) Dot blot detection of m^6A modification on mRNAs in 22Rv1 xenograft samples.

A, C, H, I, K, Data shown as means ± SD (n = 8 biological replicates). **D, F, L**, Data shown as means ± SD (n = 3 biological replicates). **G**, Data shown as means ± SD (n = 5 biological replicates). The *P* values were calculated using an unpaired two-tailed Student's *t*-test; $*P < 0.05$, $**P < 0.01$, $***P < 0.001$, n.s., not significant. Experiments in **E, M** were repeated twice.

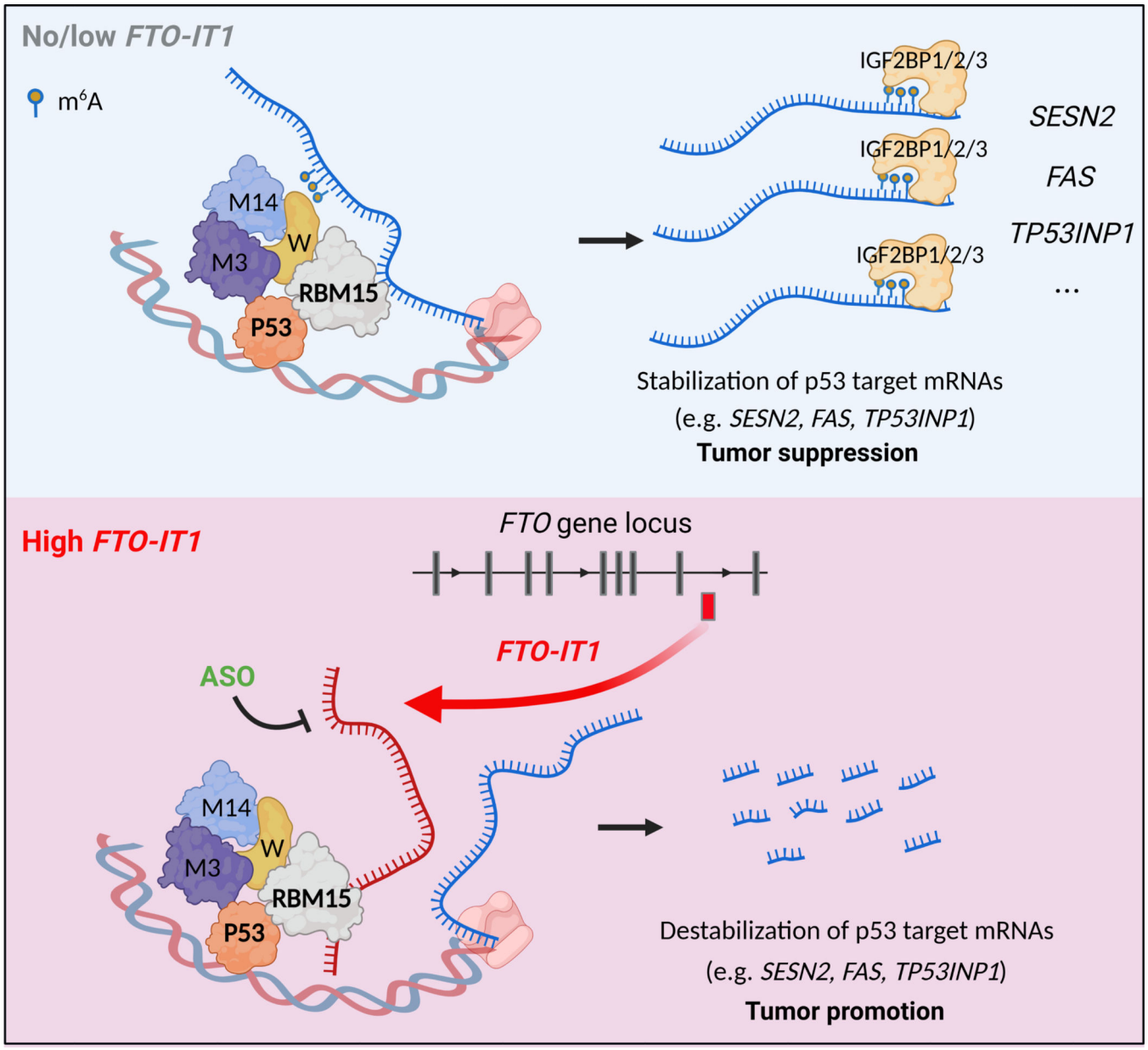

Figure 8. Proposed working model

A proposed working model for *FTO-IT1* in regulating mRNA m^{6}A methylation. Top, in cells where no/low *FTO-IT1* is expressed, RBM15 in the MTase 'writer' complex mediates the m^{6}A methylation of a subset of p53 target gene mRNAs and their stability and promotes the p53 tumor suppression functions. Bottom, overexpressed *FTO-IT1* physically interacts with RBM15 and inhibits RBM15-mediated p53 target gene mRNA m^{6}A methylation and stability, thereby attenuating p53 downstream tumor suppression signaling and tumor progression. M3, METTL3; M14, METTL14; W, WTAP.

Key Resources Table

REAGENT or RESOURCE	SOURCE	IDENTIFIER
Antibodies		
Mouse monoclonal anti-m^{6}A	Synaptic Systems	202 111
Rabbit monoclonal anti-FTO	abcam	ab126605
Rabbit polyclonal anti-METTL3	Proteintech	15073-1-AP
Rabbit polyclonal anti-METTL14	Sigma Aldrich	HPA038002
Rabbit polyclonal anti-METTL16	Proteintech	19924-1-AP
Rabbit polyclonal anti-ALKBH5	Proteintech	16837-1-AP
Rabbit polyclonal anti-WTAP	Proteintech	10200-1-AP
Rabbit polyclonal anti-RBM15	Proteintech	10587-1-AP
Rabbit polyclonal anti-RBM15B	Proteintech	22249-1-AP
Rabbit polyclonal anti-VIRMA	Proteintech	25712-1-AP
Rabbit polyclonal anti-HAKAI	Bethyl lab/ Fortis	A302-969A
Rabbit polyclonal anti-ZC3H13	Bethyl lab/ Fortis	A300-748A-T
Mouse monoclonal anti-FAS	Santa Cruz	SC-8009
Rabbit polyclonal anti-TP53INP1	Santa Cruz	SC-68919
Rabbit polyclonal anti-MDM2	abcam	ab260074
Rabbit polyclonal anti-SESN2	Proteintech	10795-1-AP
Mouse monoclonal anti-RB	BD Biosciences	554136
Rabbit polyclonal anti-P-RB T821	Invitrogen	44-582G
Mouse monoclonal anti-ERK2	Santa Cruz	SC-1647
Mouse monoclonal anti-p53	Santa Cruz	SC-126
Rabbit monoclonal anti-C-PARP1	Cell Signaling	5625S
Rabbit polyclonal anti-C-CASP3	Cell Signaling	9661S
Rabbit polyclonal anti-Ki67	abcam	ab15580
Rabbit monoclonal anti-IGF2BP1	Cell Signaling	8482S
Rabbit polyclonal anti-IGF2BP2	Proteintech	11601-1-AP
Rabbit polyclonal anti-IGF2BP3	Proteintech	14642-1-AP
Mouse monoclonal anti-BrdU	BD	555627
Goat Anti-Mouse IgG H&L (FITC)	ZENBIO	511101
Mouse monoclonal anti-Actin	Cell Signaling	3700S
Mouse monoclonal anti-MYC	Santa Cruz	SC-40
Chemicals, peptides, and recombinant proteins		
Docetaxel (DTX)	Active Biochemicals	A-1917
Enzalutamide (MDV3100)	Selleckchem	S1250
Lipofectamine 2000	Life Technologies	11668-019
Polybrene	Santa Cruz Biotechnology	sc-134220
SYBR Green Mix	Bio-Rad	170-8885

REAGENT or RESOURCE	SOURCE	IDENTIFIER
Propidium Iodide (PI)	Sigma	P4170-100mg
BrdU	Yeasen	40204ES60
Annexin V-PE apoptosis detection kit I	BD	559763
Deposited data		
RNA-seq in C4-2C and C4-2R	This paper	GEO: GSE189966
m^6A-seq in 22Rv1 cells	This paper	GEO: GSE189465
RBM15 CLIP-seq in 22Rv1 cells	This paper	GEO: GSE212043
H3K4me1 and H3K27ac ChIP-seq in VCaP cells	This paper	GEO: GSE229871
AR ChIP-seq in Mib treated C4-2 cells	Zhao et al., Cell rep 2016	GEO: GSE55032
AR ChIP-seq in ENZ treated C4-2 cells	He et al., Nat Commun 2021	GEO: GSE136130
Mass Spectrometry proteomics data	This paper	PXD041053 and 10.6019/PXD041053
Western blot raw data have been deposited in Mendeley Data	This paper	DOI: 10.17632/vs3msdvsvw.1
IFC image raw data have been deposited in Mendeley Data	This paper	DOI: 10.17632/mcnbx2pf7z.1
Experimental models: Cell lines		
HEK293T	ATCC	N/A
22Rv1	ATCC	N/A
C4-2	Uro Corporation	N/A
PC-3	ATCC	N/A
LNCaP	ATCC	N/A
LAPC4	ATCC	N/A
Breast cancer cell lines	Dr. John R. Hawse's lab	See supplementary Table 12
Experimental models: Organisms/strains		
SCID mice	Jackson Lab	N/A
Software and algorithms		
m^6A peaks analysis	Meng et al., Methods 2014	ExomePeak R package
CLIP-seq analysis	Drewe-Boss et al., Genome Biol 2018	omniCLIP
ChIP-seq analysis	Wang et al., Ann Oncol 2018	bowtie2 (version 2.2.9) and MACS2 (version 2.1.1)